PIC simulation of a ceramic-lined
Hall-effect thruster

by

Vincent Blateau

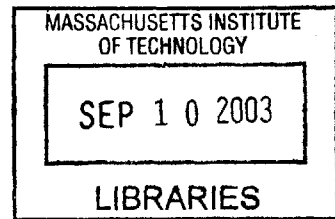Ingénieur diplômé de l'Ecole Polytechnique (2000)

Submitted to the Department of Aeronautics and Astronautics
in partial fulfillment of the requirements for the degree of

Master of Science in Aeronautics and Astronautics

at the

MASSACHUSETTS INSTITUTE OF TECHNOLOGY

September 2002

Author ....
Department of Aeronautics and Astronautics
August 23, 2002

Certified by ....
Manuel Martínez-Sánchez
Professor of Aeronautics and Astronautics
Thesis Supervisor

Certified by ....
Oleg Batishchev
Research Scientist
Thesis Supervisor

Accepted by ....
Edward M. Greitzer
Professor of Aeronautics and Astronautics
Chair, Committee on Graduate Students

AERO

PIC simulation of a ceramic-lined

Hall-effect thruster

by

Vincent Blateau

Ingénieur diplômé de l'Ecole Polytechnique (2000)

Submitted to the Department of Aeronautics and Astronautics
on August 23, 2002, in partial fulfillment of the
requirements for the degree of
Master of Science in Aeronautics and Astronautics

Abstract

A full Particle-In-Cell code, written by James Szabo [23], was used to model a 50W TAL and 3kW SPT thruster. This code treats single and double ions, neutrals and electrons as particles, moved forward by a leapfrog algorithm at each timestep, matching the lowest of the plasma and the cyclotron times. At the end of each timestep, a successive-over-relaxation algorithm solves the Gauss' formulation of the Poisson equation. Collisions include electron-neutral single and double ionization, and elastic scattering, electron-ion double ionization, ion-neutral elastic scattering and charge-exchange. A few tricks are used to decrease the computation time: superparticles, an artificial permittivity factor and lighter-than-physical ions. We modified this code to track the different components governing the thruster efficiency, and to map average internal data in the thruster. We used these tools to track changes with higher-than-nominal voltage (600, 900 and 1200V) for the 50W, 300V mini-TAL, optimizing efficiency vs. magnetic fields at each voltage. We further modified the code to model a 3kW SPT thruster. These modifications include ceramic wall secondary electron emission, a new boundary condition model for the Poisson solver at ceramic walls, an improved sheath model, and a new anomalous diffusion algorithm. Converged results with low anomalous diffusion diffusion were obtained, along with intermediary results with higher diffusion.

Thesis Supervisor: Manuel Martínez-Sánchez
Title: Professor of Aeronautics and Astronautics

Thesis Supervisor: Oleg Batishchev
Title: Research Scientist

Acknowledgments

I would like to first thank my advisors, Professor Martinez-Sanchez and Doctor Oleg Batishchev, for supporting me to fight the mysteries of the PIC code. Always available, they helped me a lot to understand results, find errors and develop solutions. I would also like to thank NASA Glenn for funding me as part of a research effort on high Isp Hall thrusters.

Among the SPL lab, my officemates, Nuria, Tatsuo, Paulo, and Jorge deserve a special thank for bearing me for a year; I am glad they are fluent in French slang by now. It was really fun working with them, I wish them good luck at MIT and after that in Japan, France, Spain, Mexico or why not America after all.

I would also like to thank my family for always supporting me, even an ocean (atlantic or pacific) away. I am looking forward to spending some time with them this summer after two years abroad.

This time at MIT would not have been the same without all my friends in Boston. From running to sailing, lunches at Rebecca's to drinks at Cambridge 1, or parties in Cambridge, I would like to thank them for being always nice and cheerful; I wish them all the best for the future.

Finally, and although they are part of the previous paragraph already, I would like to thank my three roommates, David, Guillaume, Xavier, and our extra roommate Anne-Christelle for their constant support during these two years, and for all the fun we had. We were such a great team! I am sure we will soon start recalling nice memories from Boston.

Contents

List of Figures

11

List of Tables

Chapter 1

Introduction

1.1 Electric Propulsion and Hall thrusters

Electric propulsion

The principle of electric propulsion is to use, in space, electric power as a source of energy for propulsion, instead of chemical power. The electric thrusters generate a plasma flux where ions are accelerated by an electric field. The thrust created is $F = \dot{m} < c >$, where $< c >$ is the average exit velocity.

The main advantage of that kind of propulsion is the large thrust per unit mass, or average exit velocity, that can be achieved. $\frac{F}{\dot{m}} = < c >$. This value can also be expressed in seconds as a specific impulse Isp, using $\text{Isp} \equiv \frac{F}{\dot{m}g} = \frac{<c>}{g}$, where $g = 9.81 \, m/s^2$ is the gravitational constant on earth.

In a chemical thruster, the maximum thrust per unit mass that can be achieved corresponds to the maximum chemical energy liberated by the reaction. Apart from nuclear reactions, not possible so far at such small length and mass scales, this amount is maximum for hydrogen-oxygen combustion, and corresponds to $\frac{1}{2}c^2 = E_{H20} = 13.4 \, MJ/kg$, or $c = 5174 \, m/s$. In fact, the best exit speed reached by rocket engines is of order $5000 \, m/s$,

Electric propulsion however has no such boundary, as the ions get their velocity from ΔV, the electric potential difference between their creation and the thruster

exit. For a singly-charged ion, $< c >= \sqrt{\frac{2q\Delta V}{m}}$. Thrust is proportional to $\sqrt{\Delta V}$, where ΔV is in turn proportional to the amount of power used, and can be increased with virtually no limit. This is of course neglecting many issues like heating, erosion inside and outside the thruster.

The thrust of an electric thruster is always relatively small: for a thruster to have an Isp of $1000s$, or $< c >= 10000 \, m/s$, the energy per unit mass required with a conversion efficiency of 100% is $50 \, MJ/kg$. If we assume $5kW$ is available on board a satellite for propulsion, that means a mass flow of $0.1g/s$, and a thrust of $0.5N$ only.

Hall thrusters

Hall thrusters are one of the most common type of electric thrusters. They were invented in the 1960's. The first flight took place in 1972, and the first western commercial flight is scheduled for 2002 on a geostationnary satellite. These thrusters are mainly used for station keeping, orbit re-phasing, and orbit transfer.

A Hall thruster is axysymmetric, the electric field being axial and the magnetic field, generated by coils, radial. Neutrals are injected at the anode, located at the far end of the annulus-shape chamber. Electrons are injected outside the chamber by a heated cathode. Walls are made out of metal for Thrusters with Anode Layer (TAL, Fig. 2-6), or of ceramics for Stationary Plasma Thruster (SPT, Fig. 4-1).

The electric field attracts the electrons towards the chamber, where they are trapped in a Larmor motion. They drift azymuthaly in the annulus chamber due to the $\vec{E} \times \vec{B}$ drift. The Larmor motion and the drift increase tremendously the electron mean path, which becomes of the same order as the ionization collisions mean free path. Ions created are accelerated by the field towards the exit of the thruster; due their higher mass, they are not magnetized.

There is a wide range of Hall thrusters available with powers from a few hundred Watts to 8kW, thrust from 30mN to 500mN. The most common operating voltage used is $300 \, V$. Two macroscopic numbers characterize the performances of Hall thrusters: the specific impulse, Isp $= \frac{F}{\dot{m}g}$ and the anode efficiency, $\eta = \frac{F^2}{2\dot{m}\Delta VI}$. Typical values are $1,700 \, s$ to $2,000 \, s$ for the Isp, and 0.5 to 0.6 for the anode efficiency.

1.2 Hall thruster modeling

Many efforts have been done over the last decade to model Hall thrusters. One-dimensional and two-dimensional models have been developed. These codes help understand the physics going on in the Hall thrusters, and are able to produce data, such as near-wall conductivity, or electron energy distribution function that cannot be measured in experiments.

Using a 1D linear model, Noguchi, Martinez-Sanchez and Ahedo [14] obtained the axial oscillations observed in SPT thrusters. Ahedo, Martinez-Cerezo, Gallardo, and Martinez-Sanchez [1] have developed a 1D analytic steady model that includes heat conduction and lateral wall interaction such as recombination, energy losses, or near-wall conductivity. They noticed a narrow range of magnetic field where steady solutions can be found.

Fife [6] built a 2D (R, Z) hybrid-PIC code where electrons are modeled as a Maxwellian fluid. Bohm diffusion is included, and wall effects are calculated as a function of the electron temperature. Neutrals and ions however are modeled with a particle-in-cell scheme. He modeled the SPT-100 thruster, and Szabo [25] modified his code to model the Busek-BHT-200-X2 SPT thruster. Predicted results agree well with experiments, with a 70% lower Bohm diffusion than the classical $\frac{1}{16}\frac{kT_e}{eB}$.

Still, the electron energy distribution function of the electrons in Hall thrusters had been found to depart from a Maxwellian towards a "double-hump" shape distribution [2]. Szabo [23] developed a full-PIC code at MIT for his PhD degree. This model, detailed more precisely in chapter 2, includes a particle-modeling for electrons, single and double ions and neutrals. This code was originally designed to model the 50W mini-TAL thruster, designed at MIT by Khayms [12]. Results agree with experiments within 20 to 33 percent, and a design error in the mini-TAL magnetic field was found, explaining the very low efficiency found in experiments. The electron population was found to be non-Maxwellian with temperature gradients along the magnetic lines.

1.3 Objectives

There is increased interest in extending the range of mission applicability of Hall thrusters through increases in their operating specific impulses, and, if possible, of their efficiency [16]. This work aims at better understand the behavior of TAL and SPT thrusters, through simulation, using Szabo's PIC code [23]. Chapter 2 describes the principles of the code, dividing it into 4 sections: the electro-magnetic part, the collisions, the boundary conditions, and the tricks used to decrease the computation time. Chapter 2 describes results of the PIC code for the mini-TAL at high voltage, both on the macroscopic and on the local scales, and identifies trends versus voltage. Chapter 3 explains the modifications made to the code to model the P5 SPT thruster, problems encountered and corresponding solutions, along with preliminary results.

Chapter 2

The PIC Code

2.1 Generalities about the PIC Code

The purpose of the present code, developed by James Szabo at MIT [23], is to model a Hall-effect thruster. A good way to model such a plasma is to use a Particle-In-Cell (PIC) method. The idea of the PIC method is to have lists of particles (neutrals, electrons, ions for this full-PIC code) with their geometric location and velocities on one side, and a grid on the other side, used to solve numerically the electro-magnetic field. The link between the particles and the field is performed at each timestep by interpolating the electro-magnetic force at the particle location, and by the weighting of the charges on the grid node after moving it. The electric potential, and then the electric field are calculated from the charge distribution, and the electric boundary conditions; the particles are pushed forward using a numerical integration of the equations of motion. This procedure is explained in more detail in figure 2-1, and section 2.2.

Ideally the simulation domain should be 3-dimensional. To reduce the required computation time, this code neglects variations in the azimuthal direction in space, hence neglecting any azimuthal oscillations. The particles have three dimensions in velocity, but are all assumed to be in a ($\theta = 0$) plane. When a particle is stepped forward, it is assumed to remain in the simulation plane, and only its axial, z, and radial, r, coordinates are stored.

Acceleration & Move

Vnew = Vold + qE/m dt

Xnew = Xold + Vnew dt

"Interpolation"

E

"Assignment"

ρ

Poisson's equation (SOR)

$\Delta\Phi = -\rho/\varepsilon$

Maxwell's equation

$\mathbf{E} = -\nabla\Phi$
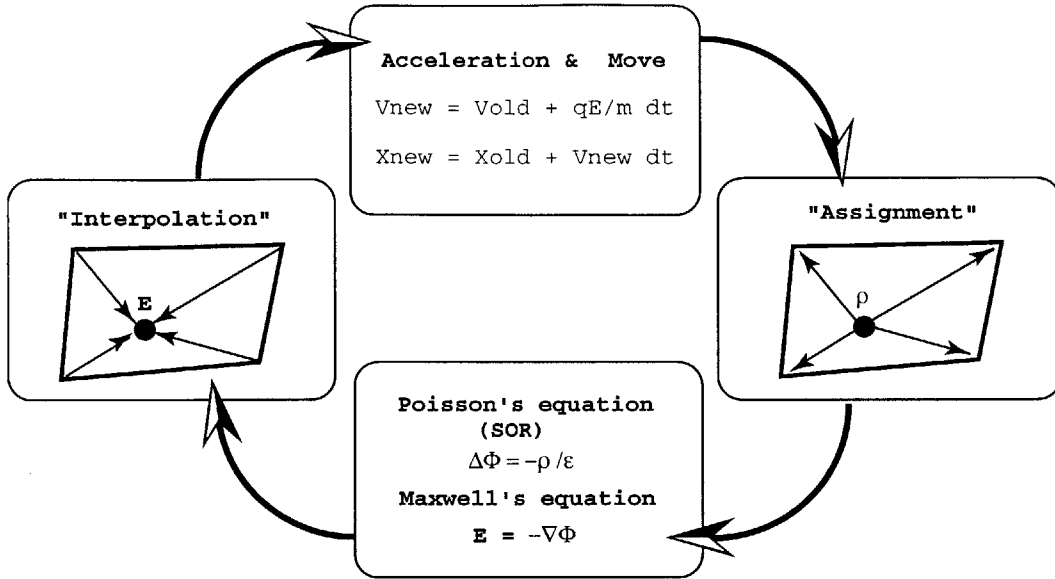
Figure 2-1: The PIC method (courtesy of Tatsuo Onishi)

Two tricks are used to decrease the computation time: an artificial permittivity constant $\gamma^2\epsilon_0$, where γ^2 is the artificial ratio, and an artificial mass ratio for the heavy neutrals. The artificial permittivity constant decreases the plasma frequency and the physical scale of the electro-magnetic phenomena, hence increasing the computation timestep, and the required grid spacing for the electric solver. On the other hand, the artificial mass ratio, by speeding up the heavy particles, decreases the number of iterations allowable to reach convergence. These coefficients help decrease the simulation time, but also imply many scaling changes in the code. To get a better idea of what they mean in the computation, they are first ignored in sections 2.2 to 2.4, their combined effects are then explained in section 2.5.

This chapter gives an overview of the physics in the model, applied to the mini-TAL thruster. More details on the model and on the mini-TAL can be found in [23]. In fact, the thruster used in this model is a modified version of the mini-TAL, as explained in [23, section 5.9.2]. Modifications to the code and application to the P5 thruster are treated in chapter 4.

The model is subdivided into three different parts, described in sections 2.2 to 2.4:

- the interaction between the electro-magnetic field and the plasma

- the collisions inside the plasma

- the particle-wall interaction

The notations used are the same as in [23], the axial and radial dimension of the thruster are called z and r, the same dimensions in grid coordinates are called ξ and η for real numbers, and k and j for integers defining a cell or a node.

2.2 Electro-Magnetic part of the code: Poisson solver and leapfrog algorithm

The interactions between the electro-magnetic field and the plasma are very important as the field is the energy source for the thruster. The effects of the particles on the field are explained in section 2.2.1; the effects of the field on the particles are described in section 2.2.3. The independent pre-computed magnetic field is shown in section 2.2.2.

2.2.1 The Poisson solver

Equation to solve

The full Maxwell equations governing the electro-magnetic field in the simulation region are:

$$\vec{\nabla}.\vec{E} = \frac{\rho}{\epsilon_0} \tag{2.1}$$

$$\vec{\nabla} \times \vec{B} = \mu_0\vec{j} + \mu_0\epsilon_0\frac{\partial \vec{E}}{\partial t} \tag{2.2}$$

$$\vec{\nabla} \times \vec{E} = -\frac{\partial \vec{B}}{\partial t} \tag{2.3}$$

$$\vec{\nabla}.\vec{B} = 0 \tag{2.4}$$

where $\rho = -e(n_e - n_i)$ is the charge density.

The induced magnetic field due to the real current, $\vec{j}$, and due to the displacement current $\vec{j}_d = \mu_0 \epsilon_0 \frac{\partial \vec{E}}{\partial t}$ can be evaluated:

$$\left[\vec{\nabla} \times \vec{B}_{ind1} \right] = \frac{B_{ind1}}{L} = \left[\mu_0 \vec{j} \right] = \mu_0 \frac{I}{L^2} \tag{2.5}$$

$$\frac{B_{ind2}}{L} = \left[\epsilon_0 \mu_0 \frac{\partial \vec{E}}{\partial t} \right] = \epsilon_0 \mu_0 \frac{\Delta V}{L} f_{comp} \tag{2.6}$$

For a mini-TAL thruster, $P = 50mW$, $\Delta V = 300V$, $I = 6mA$, $B_{min} \simeq 0.2T$, $f_{comp} = 2.2 \times 10^{10} Hz$ (from section 2.2.4),

$$B_{ind1} = \mu_0 \frac{I}{L} \simeq 7.5 \times 10^{-6} T \tag{2.7}$$

$$B_{ind2} = \epsilon_0 \mu_0 \Delta V f_{comp} \simeq 7.4 \times 10^{-5} T \tag{2.8}$$

The B-field created by the magnets is much larger than the induced B-field created. Neglecting the induced B-field, the Maxwell equations become:

$$\vec{\nabla}.\vec{E} = \frac{\rho}{\epsilon_0} \tag{2.9}$$

$$\vec{\nabla} \times \vec{B} = 0 \tag{2.10}$$

$$\vec{\nabla} \times \vec{E} = 0 \tag{2.11}$$

$$\vec{\nabla}.\vec{B} = 0 \tag{2.12}$$

The rotational of $\vec{E}$, $\vec{\nabla} \times \vec{E}$, being zero everywhere in a compact larger than the thruster itself, we can write $\vec{E}$ as $\vec{E} = -\vec{\nabla}\phi$, where ϕ, the electric potential, is defined by the boundary conditions and the Poisson equation

$$\Delta\phi = \frac{\rho}{\epsilon_0} \tag{2.13}$$

Which is the equation to solve to calculate the potential in the domain.

Solving the equation: the Gauss method

The Poisson equation (2.13) cannot be solved analytically, this section explains how to discretize the equation before solving it numerically.
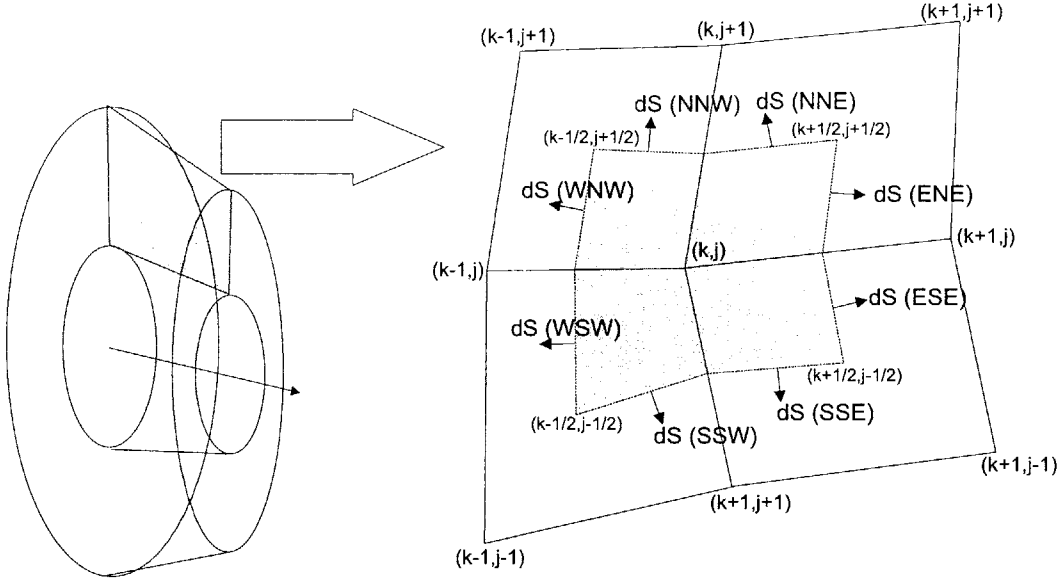
Figure 2-2: Gauss' theorem applied at a node of the simulation region

The idea is to apply Gauss' theorem to $\vec{\nabla}.\vec{E} = \frac{\rho}{\epsilon_0}$ (2.9):

$$\oint_{\text{control volume}} \vec{E}.d\vec{S} = \frac{Q}{\epsilon_0} \qquad (2.14)$$

where $Q = \oint_{\text{control volume}} \rho.dV$ is the total charge inside the control volume.

We can apply that formula at each node inside the simulation domain, defining as a control volume a "ring", whose intersection with the $\theta = 0$ plane is an 8-sided polygon, delimited by the center of the four cells around node (k, j), and the four centers of the segments between the central node and its 4 adjacent nodes (Fig. 2-2). The simulation is still two-dimensional, but as explained in section 2.1, the azimuthal invariance enables us to account for the 3D space. The method used by James Szabo [23] was using only 4-sided polygons defined by the 4 cell centers. Due to the higher mesh distortion in the P5 thruster as shown in Fig. 4-5, we changed it to the 8-sided polygon method.

Applying Eq. (2.15) to the defined control-volume,

$$\oint_{\text{control volume}} \vec{E}.d\vec{S} = \Sigma_{\text{i, 8 faces}} \oint_{\text{surface i}} \vec{E}.d\vec{S}_i = \frac{Q}{\epsilon_0} \qquad (2.15)$$

The $\vec{E}$ term can be expressed as a function of the potential, in cylindrical coordi-

nates:

$$\vec{E} = -\vec{\nabla}\phi = -\left(\frac{\partial\phi}{\partial z}\vec{i_z} + \frac{\partial\phi}{\partial r}\vec{i_r} + \frac{1}{r}\frac{\partial\phi}{\partial\theta}\vec{i_\theta}\right) \tag{2.16}$$

and, using the grid coordinates,

$$\frac{\partial\phi}{\partial z} = \frac{\partial\phi}{\partial\xi}\frac{\partial\xi}{\partial z} + \frac{\partial\phi}{\partial\eta}\frac{\partial\eta}{\partial z} \tag{2.17}$$

$$\frac{\partial\phi}{\partial r} = \frac{\partial\phi}{\partial\xi}\frac{\partial\xi}{\partial r} + \frac{\partial\phi}{\partial\eta}\frac{\partial\eta}{\partial r} \tag{2.18}$$

Equations (2.17) and (2.18), substituted in Eq. (2.16) can be used in Eq. (2.15), to get an analytic expression between the derivatives of phi and the local charge:

$$\oint_{\text{control volume}} \vec{E}.d\vec{S} = \Sigma_{i,\ 8\ \text{faces}} \left[\oint_{\text{surface i}} \begin{pmatrix} \frac{\partial\phi}{\partial\xi}\frac{\partial\xi}{\partial z} + \frac{\partial\phi}{\partial\eta}\frac{\partial\eta}{\partial z} \\ \frac{\partial\phi}{\partial\xi}\frac{\partial\xi}{\partial r} + \frac{\partial\phi}{\partial\eta}\frac{\partial\eta}{\partial r} \\ 0 \end{pmatrix} .d\vec{S_i} \right] \tag{2.19}$$

So far, we have not introduced any approximation. Now, we need to approximate each term of integral (2.19). That means approximating, for each of the 8 segments:

- $\frac{\partial\xi}{\partial z}, \frac{\partial\xi}{\partial r}, \frac{\partial\eta}{\partial z}, \frac{\partial\eta}{\partial r}$

- $\frac{\partial\phi}{\partial\xi}, \frac{\partial\phi}{\partial\eta}$

- $d\vec{S_i}$

The original code used 4-sided polygons (North, East, South and West), using both first and second-order approximations for the derivatives listed above. We rewrote that part of the code to include the 8 polygons and second-order developments. This tedious work is done in subroutine *consolidate()*, written in appendix B. *consolidate()* calculates for each node the 9 constants by calling several times *gauss_dielectric()*. *gauss_dielectric()* calculates itself the components for a North-East corner configuration, hence inputs and outputs to that function have to be adjusted for other corners.

Plugging in all the 8 surfaces, we get a final expression for the Poisson equation at node (k,j), of the form:

$$C\phi_{k,j} + E\phi_{k+1,j} + NE\phi_{k+1,j+1} + N\phi_{k,j+1} + NW\phi_{k-1,j+1} + W\phi_{k-1,j} +$$
$$SW\phi_{k-1,j-1} + S\phi_{k,j-1} + SE\phi_{k+1,j-1} = \frac{Q_{k,j}}{\epsilon_0} \tag{2.20}$$

24

This is the linear equation we are going to solve in section 2.2.1. Each of the 9 coefficients of each node in the simulation are geometric coefficients, and need to be computed only once.

The SOR algorithm

We now have a discretized equation to solve. The method to actually solve it is an iterative method called Successive-Over-Relaxation (SOR). At each iteration i, we calculate for each node a "half-step" potential $\phi_{k,j}^{i+0.5}$ defined by:

$$
\begin{aligned}
\phi_{k,j}^{i+0.5} = \frac{1}{C}(&-E\phi_{k+1,j}^i - NE\phi_{k+1,j+1}^i - N\phi_{k,j+1}^i - NW\phi_{k-1,j+1}^i \\
&-W\phi_{k-1,j}^i - SW\phi_{k-1,j-1}^i - S\phi_{k,j-1}^i - SE\phi_{k+1,j-1}^i + \frac{Q_{i,j}}{\epsilon_0})
\end{aligned} \quad (2.21)
$$

This "half-step" potential is used to calculate the "full-step" potential according to:

$$
\phi_{k,j}^{i+1} = \phi_{k,j}^i + \omega(\phi_{k,j}^{i+0.5} - \phi_{k,j}^i) \quad (2.22)
$$

Convergence is governed by the maximum of the right-hand-side terms of a given iteration:

$$
max_{k,j}\{RHS_{k,j}^i\} = max_{k,j}\{\left(\phi_{k,j}^{i+0.5} - \phi_{k,j}^i\right)\} \quad (2.23)
$$

The value of ω can be adjusted to increase the computation speed. For the mini-TAL, a value of 1.96 is optimum, and machine-level precision can be reached in 800 iterations. This calculation is done at each iteration of the PIC code.

Boundary conditions for the Poisson solver

The Poisson equation (2.15) and its numerical approximation (2.20) are valid for the bulk of the plasma. For a boundary point, we need either the value of $\phi_{k,j}$ itself, in which case we do not need to solve an equation for the node, or the value of $\vec{E}.d\vec{S}$ at the edge of the boundary. As shown in figure 2-3, we can indeed reduce the size of the control volume, up to the boundary itself, and that leaves only one requirement for the boundary condition: the value of $E_\perp$. The curvature of the boundary at each control volume is neglected as the curvature radius is much larger than a cell width.

In the simulation of a TAL, we have four kinds of boundaries:
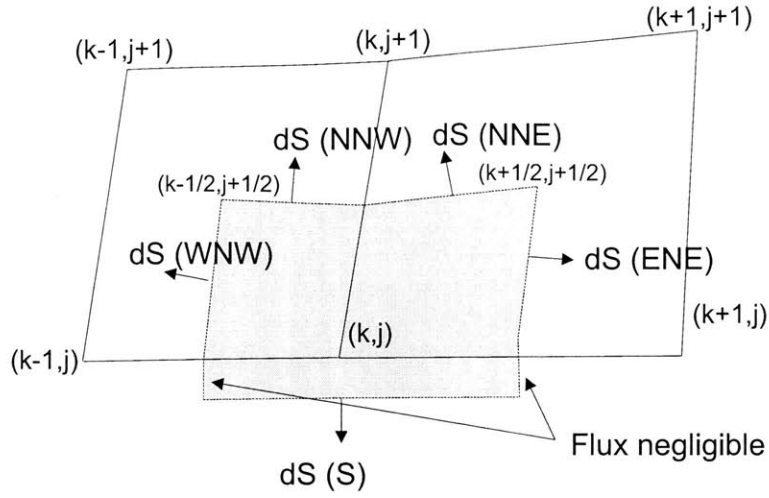
Figure 2-3: Gauss' theorem applied at a node on a boundary

- Metallic walls at fixed potential.

  This is the easier case, the potential is already set.

- Metallic walls at floating potential

  The potential along a metallic wall is constant, but its value relative to the cathode can change. We assume that the plasma on one side, and the spacecraft materials on the other side, are insulators, and therefore the wall potential is determined as a capacitor's potential: $\phi = \frac{Q_{wall}}{C}$.

  The value of C is of relative importance only, as the wall potential is adjusting to reach null net charge balance at the wall. Still, the charging time has to be larger than the smallest timestep in the system, and not too high (less than 1000 timesteps) so that the wall reaches equilibrium. That charging time t_{charge} can be estimated using:

  $$C\Delta\phi = \Delta Q_{wall} = t_{charge} \oint j_{wall} dS_{wall} = t_{charge} e n_i v_{Bohm} S_{wall} \quad (2.24)$$

- Centerline

  At the centerline, to insure continuity of ϕ, $\frac{\partial E}{\partial r} = 0$ is required.

- Free-space boundary

At the free space boundary, we can assume either $\phi \simeq 0$, or $E_\perp \simeq 0$. The less-constraining of the two possibilities is setting $E_\perp$, as the plasma is supposed to be quasi-neutral outside the chamber. This is the condition that is used in the results of the following chapters.

An added constraint is used at this boundary: a limit on the negative value at the boundary. If the calculated potential during the convergence process of the Poisson solver happens to be less than, say $10V$, below the cathode potential, at a free space boundary, the code limits it to $\phi_{cathode} - 10V$. This means replacing temporarily the condition $E_\perp = 0$ by a condition on ϕ, and is justified by the fact that no electrons, and therefore no plasma, should be able to make it to a region with a potential lower than that of the cathode.

2.2.2   The magnetic field

The magnetic field in the thruster is assumed to be constant, as explained in section 2.2.1. It is therefore pre-computed by a commercial software package like Maxwell, using the magnet configuration, then loaded and interpolated by the code to its own grid. As shown on Fig. 2-4, the magnetic field of Hall-effect thrusters is mostly radial, in order to have a drift velocity along the azimuthal direction.

2.2.3   The leapfrog algorithm

In a Hall thruster, charged particles undergo electro-magnetic forces. Ions see mostly the electric field, due to their high mass (the magnetic force per unit mass is proportional to $\frac{q}{m}\vec{v} \times \vec{B}$), whereas electrons are trapped in a Larmor motion around magnetic lines, and drift in the $\vec{E} \times \vec{B} = \vec{i_\theta}$ direction.

The exact equations of motion and the leapfrog method

The equations of motion for a charged particle, neglecting any collision or diffusion effect is:

$$m\frac{d\vec{v}}{dt} = q(\vec{E} + \vec{v} \times \vec{B}) \tag{2.25}$$
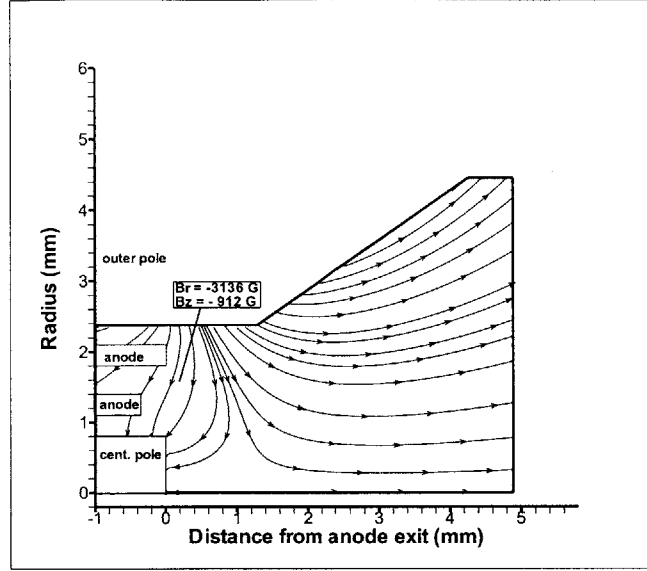
Figure 2-4: Nominal magnetic field for the mini-TAL thruster

$$\frac{d\vec{x}}{dt} \;=\; \vec{v} \tag{2.26}$$

The code works with timesteps, the leapfrog algorithm as described by Birdsall [5], takes care of updating the velocity and moving the particle forward. This means integrating numerically (2.25) and (2.26) over a timestep.

First, it calculates $\vec{v}_{i+1}$, the velocity at timestep $i + 1$, and uses that velocity in a second time to calculate, $\vec{x}_{i+1}$, the particle position at t_{i+1}. This is why it is called leapfrog algorithm. The error due to an explicit scheme is of order δt, and Birdsall recommends to have $\omega_{max}\delta t \leq 0.3$, where ω_{max} is the highest angular frequency.

Calculating the new velocity

To calculate $\vec{v}_{i+1}$ we need to integrate (2.25) where $\vec{v}$ is present on both sides. The method of Boris is used: it consists of integrating over half a timestep using the electric field force only, then over a full timestep with the magnetic field, and finally with the electric field over half a timestep again. More details can be found in [5] or [23, section 3.14]. Throughout this calculation, we are going to work in the local cylindrical basis at $\vec{x}_i$, (i_z, i_r, i_θ) where $\vec{E}$ and $\vec{B}$ have no component along i_θ.

28

First, applying half a timestep in electric field:

$$\vec{v}^- = \vec{v} + K\vec{E}, \text{where } K = \frac{q\Delta t}{2m} \tag{2.27}$$

Then, applying the full timestep in magnetic field, $\vec{v}^+$ is the solution of :

$$\vec{c} = \vec{v}^- + K\vec{v}^- \times \vec{B} = \vec{v}^+ - K\vec{v}^+ \times \vec{B} \tag{2.28}$$

Solving for $\vec{v}^+$,

$$\vec{v}^+ = \begin{pmatrix} c_r - KB_z v_\theta^+ \\ c_z + KB_r v_\theta^+ \\ \frac{c_\theta + KB_z c_r - KB_r c_z}{1 + K^2 B_z^2 + K^2 B_r^2} \end{pmatrix} \tag{2.29}$$

Finally, adding the second half-timestep of electric field:

$$\vec{v}_{i+1} = \vec{v}^+ + K\vec{E} \tag{2.30}$$

In any of these formulas, $\vec{E}$ has a zero component along the third axis: the θ direction.

The velocity we have calculated here is the velocity at timestep t_{i+1} in the local cylindrical basis of location $\vec{x}_i$. After we move the particle forward, we will have to calculate the new velocity's components in the new basis.

Moving the particle

Once the new velocity is calculated, the particle is moved using the new velocity. Linearizing Eq. (2.26):

$$\vec{x}_{t_{i+1}} = \vec{x}_{t_i} + (t_{i+1} - t_i)\,\vec{v}_{t_{i+1}} \tag{2.31}$$

The new location of the particle is the following:

$$r_{i+1} = \sqrt{(r_i + v_{r,i+1}\Delta t)^2 + (v_{\theta,i+1}\Delta t)^2} \tag{2.32}$$

$$z_{i+1} = z_i + v_{z,i+1} \tag{2.33}$$

Finally, we need to calculate the velocity in the new basis, which will be needed at the next iteration.
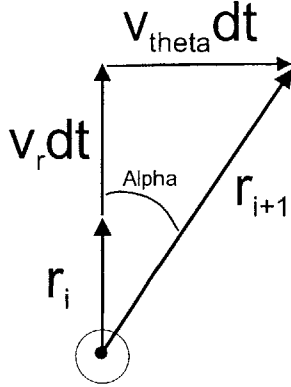
Figure 2-5: Calculating the new radius

The exact expression of $\vec{v}_{i+1}$ in the new basis is the following:

$$\vec{v}_{i+1} = \begin{pmatrix} \cos\alpha\, v_{r,i+1} + \sin\alpha\, v_{\theta,i+1} \\ v_{z,i+1} \\ -\sin\alpha\, v_{r,i+1} + \cos\alpha\, v_{\theta,i+1} \end{pmatrix} \tag{2.34}$$

In the code, the *cos* and *sin* functions do not need to be calculated, they can be calculated from dr, dz and r_{i+1}:

$$\cos\alpha = \frac{dz}{r_{i+1}} \tag{2.35}$$

$$\sin\alpha = \frac{dr}{r_{i+1}} \tag{2.36}$$

2.2.4 Grid design and timestep requirements

Grid design

A grid is required for the electro-magnetic part of the code. The grid spacing has to match the Debye length $\lambda_d = \sqrt{\frac{\epsilon_0 kT_e}{e^2 n_e}} \simeq 9\mu m$ with $n_e = 1 \times 10^{13}\, cm^{-3}$ and $Te = 15\, eV$ to capture these effects. That would mean for the 5 mm-long mini-TAL a 1000×1000 grid, which is impossible for the Poisson solver to handle. As explained in section 2.5.2, an artificial permittivity increases numerically that length by a factor of 10, the grid dimension (Fig. 2-6) decreasing to 87×49.
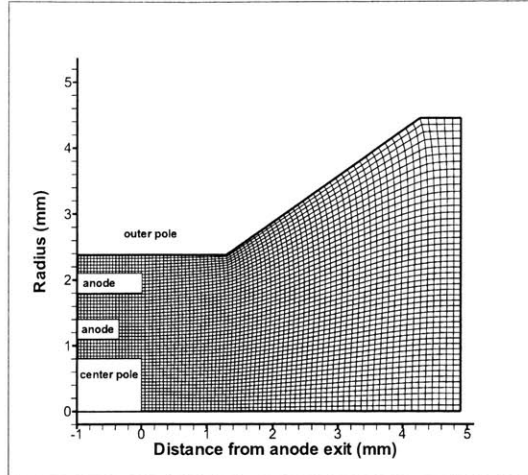
Figure 2-6: Mini-TAL grid

Orthogonality for the grid is not required, as we are not neglecting the cross derivatives terms in Eq. (2.19).

Timestep

The effects we have to capture are the plasma oscillations and the electron Larmor motion. Frequencies for ions and neutrals are much lower because of their higher mass.

$$f_p = \frac{\omega_p}{2\pi} = \frac{1}{2\pi\gamma}\sqrt{\frac{e^2 n_e}{m_e \epsilon_0}} \simeq \frac{1}{\gamma} \times 2 \times 10^{10} Hz \tag{2.37}$$

$$f_c = \frac{\omega_c}{2\pi} = \frac{1}{2\pi}\frac{qB}{m_e} \simeq 2.2 \times 10^{10} Hz \text{ for } B_{max} = 0.7T \tag{2.38}$$

Using $\omega_{max}\delta t = 0.3$, as recommended by Birdsall, the timestep is of the order of $\frac{0.3}{2\pi \, max(f_p, f_c)} \simeq 2.6 \times 10^{-12}s$, limited by ω_c.

One thing required by the PIC method is that the interpolation process be accurate, hence the particle should not move more than one cell at a time. With a timestep of $2.6 \times 10^{-12}s$ and an electron velocity of order $4 \times 10^6 m/s$ $(10\,eV)$, $\Delta x \simeq 0.01\,mm$; this is less than a cell length ($\simeq 0.05\,mm$).

31

2.3 Collisions

Collisions in a Hall thruster are responsible, among other things, for plasma pro-
duction through ionization, and some of the cross-field electron diffusion. To decide
which collisions should be included in the code, it is necessary to look at the mean
free paths.

Section 2.3.1 defines what a mean free path means, section 2.3.2 calculates the
mean free paths for the mini-TAL, and section 2.3.3 explains how the collisions are
implemented.

2.3.1 Definition of a mean free path

The collision rate for one collision type between particles of type 1 and 2 is:

$$R_{12} = n_1 n_2 v_{12} Q_{12} \qquad (2.39)$$

The collision rate for one particle of type 1 is $\nu_{12} = n_2 v_{12} Q_{12}$, and its mean free path:

$$\lambda_1 = \frac{v_1}{\nu_{12}} = \frac{1}{n_2 Q_{12}} \frac{v_1}{v_{12}} \qquad (2.40)$$

If 1 is much faster than 2 (for instance if 1 is an electron and 2 a neutral), then
$\lambda_1 \simeq \frac{1}{n_2 Q_{12}}$. On the contrary, if 2 is much faster than 1, then $\lambda_1 \simeq \frac{1}{n_2 Q_{12}} \frac{v_1}{v_2}$.

For each phenomenon, we can calculate a mean free path. It should ideally be
computed using the distribution function for the velocity difference v_{12}, but for the
order of magnitude number, we just take a value at the peak of the velocity distribu-
tion function. Then, the code compares it to the actual path of particles, which is of
the order of the thruster axial length for heavy non magnetized particles (neutrals,
ions), but of the order of a meter for the electrons, trapped in Larmor motion by the
magnetic field, and drifting around the axis.
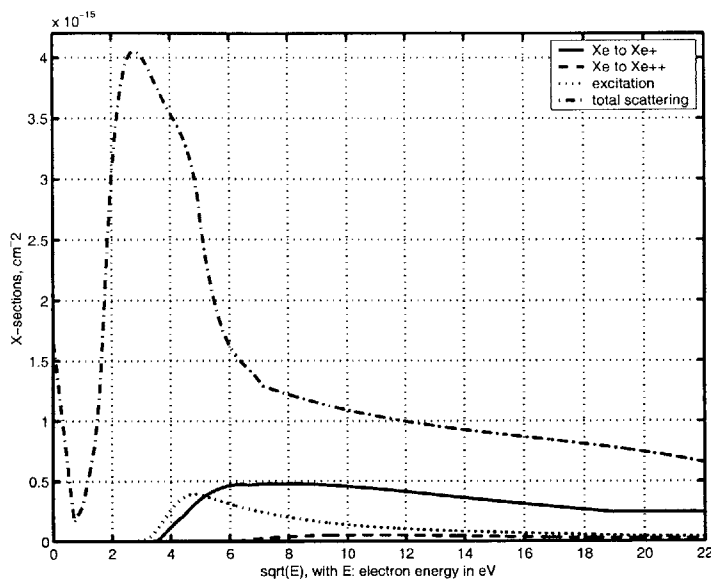
Figure 2-7: Cross-sections between electron and neutrals

2.3.2 Mean free path analysis

Electron-Neutral collisions

The three phenomena taking place between electrons and neutrals are elastic scattering, excitation, and ionization.

The cross-sections used, as shown on figure (2-7), are polynomial fits from experimental data by Ramsauer [18], Ramsauer and Kollath [19], Rapp and Englander-Golden [20]. For an electron of energy $10\,eV$, with $n_n = 5 \times 10^{13}\,cm^{-3}$ (value after the ionization region), $\lambda_{total} \simeq 5\,cm$. This is much smaller than the actual electron path, which should be of the order of a meter, even for the mm-scale mini-TAL. Out of the three phenomena, none of them is negligible; the elastic scattering is the most frequent, but the ionization and excitation reach up to 40% of the total cross section at higher energies.

Electron-Ion non-Coulomb collisions

Although the cross-section for double-from-single ionization is small (Fig. 2-8), its peak value being $2.5 \times 10^{-16}\,cm^2$, and the ion density, $1 \times 10^{13}\,cm^{-3}$ is much smaller

33
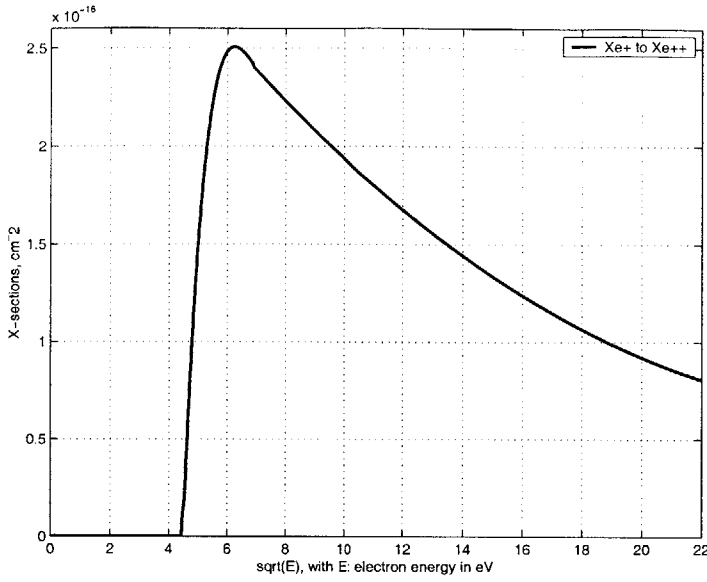
Figure 2-8: Cross-sections between electron and single ions

than the neutral density, the mean free path for an electron for double-from-single ionization is $\lambda \simeq 400\,cm$. These collisions are included, but single ion excitation is not modeled.

Ion-Neutral collisions

Ion-Neutral collisions consist of charge exchange and elastic scattering.

Charge-exchange: The cross section for charge exchange from Rapp and Francis [21], is:

$$Q_{cex} = (k_1 \log c_r + k_2)^2 \times 10^{-16}\,cm^2 \tag{2.41}$$

with $k_1 = -.8821$, $k_2 - 15.1262$, c_r in m/s. Neutrals are much slower than ions, and if we assume that the ion speed is of the order of the sonic speed $\sqrt{\frac{kT_e}{m_i}}$, for $T_e = 10\,eV$, $Q_{cex} \simeq 6.64 \times 10^{-15}\,cm^2$.

For an ion (fastest species), in the mini TAL, the neutral density before the ionization region is of the order of $n_n \simeq 7 \times 10^{14}\,cm^{-3}$,

$$\lambda_{cex,i} \simeq \frac{1}{n_n Q_{cex}} \simeq 0.21\,cm \tag{2.42}$$

34

This mean free path increases after the ionization region, following the neutral density drop.

For a neutral, assuming the neutrals have a temperature of order $0.1\,eV$, and $n_i \simeq 10^{13}\,cm^{-3}$

$$\lambda_{cex,n} \simeq \frac{1}{n_i Q_{cex}} \frac{v_n}{v_i} \simeq 1.51\,cm \tag{2.43}$$

The mean free paths of the charge-exchange collisions are of the same order of magnitude as the thruster size. They are still included, as they are responsible for interesting effects like sputtering outside the main beams. Besides, these collisions are much more important in larger thruster like the P5 (see section 4.1).

Ion neutral elastic scattering:

The cross section for elastic scattering is, from [15]

$$Q_{in,scat} = \frac{8.28072 \times 10^{-10}}{c_r}\,cm^2 \tag{2.44}$$

where c_r is the relative speed between the ion and the neutral in cm/s. using the same numbers as for the charge exchange collisions,

For an ion,

$$\lambda_{scat,i} \simeq \frac{1}{n_n Q_{scat}} \simeq 0.49\,cm \tag{2.45}$$

For a neutral,

$$\lambda_{scat,n} \simeq \frac{1}{n_i Q_{scat}} \frac{v_n}{v_i} \simeq 3.42\,cm \tag{2.46}$$

These collisions are included in the simulation, they can be switched off to reduce the computation time.

Neutral-Neutral scattering

From [15], the cross-section for neutral-neutral scattering is

$$Q_{n,n} = 2.117 \times 10^{-14} c_r^{-0.25}\,cm^2 \tag{2.47}$$

where c_r is in m/s. Again, with $T_n = 0.1\,eV$, and $n_n = 7 \times 10^{14}\,cm^{-3}$,

$$\lambda_{n,n} \simeq \frac{1}{n_n Q_{n,n}} \simeq 0.3\,cm \tag{2.48}$$

These collisions aref not included, as the neutral population is not the main species the code studies. Still, neutrals are the substrate for ionization, and neutral-neutral scattering has, along with wall interaction, an important role in neutral diffusion. These collisions should be included in a further development of the code.

Coulomb collisions

Coulomb collisions are implemented in the code, both using a Monte-Carlo approach [23, section 3.15.4] and a Fokker-Plank approach [23, section 3.16]. As they are low angle, and of relatively low cross sections in the main area of interest: the chamber, where the temperature is high, they do not bring significant changes in the results. These collisions are switched off.

Bulk recombination

The recombination rate for single ions is:

$$\dot{n}_{rec} = \alpha n_e n_i \tag{2.49}$$

where $\alpha = 1.09 \times 10^{-20} n_e T^{-\frac{9}{2}} \frac{m^3}{s}$.

This formula agrees with experiments for temperature below $3000K$, and over-predicts the real recombination rate for higher temperatures. For $T_e = 3000K$, $n_e \simeq 1 \times 10^{13} \, cm^{-3}$, $\dot{n}_{rec} \simeq 2.46 \times 10^{15} \, cm^{-3} s^{-1}$.

This rate can be compared to the ionization rate: the mass flux of the thruster is $0.13 mg/s \simeq 5.9 \times 10^{17} particles/s$, the ionization efficiency of order 0.75, and the volume $\pi r^2 L \simeq .063 \, cm^3$, the average ionization rate is hence of the order: $7.0 \times 10^{18} \, cm^{-3} s^{-1}$. It is three order of magnitude higher than the recombination rate, recombination is neglected.

Anomalous diffusion

Another important effect that takes place in the plasma is anomalous diffusion. This matter is discussed in more detail in [23, section 2.2.3].

As explained in section 2.2.3, electrons are trapped in Larmor motion and therefore drift around the axis, move up and down the magnetic field line but do not normally cross these lines in the (z,r) plane, except through the collision events.

The diffusion across the magnetic field due to collisions in the plasma is

$$D_\perp = \frac{kT_e}{m_e} \frac{1}{\omega_c} \frac{\beta}{1 + \beta^2} \tag{2.50}$$

where $\beta = \frac{\omega_c}{\nu}$ is the Hall parameter, and measures the magnetization of the plasma. ω_c is the cyclotron frequency, and ν is the collision frequency for an electron. If $\beta >> 1$, the plasma is fully magnetized, if $\beta << 1$, the plasma is governed by collisions.

Eq. (2.50) shows a $\frac{1}{B^2}$ dependence of $D_\perp$, however cross-field diffusion measurements from experiments vary as $\frac{1}{B}$. This higher diffusion, called Bohm diffusion is well approximated by the formula:

$$D_\perp = \frac{1}{16} \frac{kT_e}{eB} \tag{2.51}$$

The way this diffusion is originally modeled in the code is by increasing artificially the collision rate. A new kind of collisions is created: the "Bohm" collisions, which only randomize the direction of the electron velocity in the $B_\perp$ plane. The "Bohm" collision frequency ν_B is calculate by solving Eq. (2.52) for $\beta = \frac{\omega_c}{\nu_{regular} + \nu_B} \simeq \frac{\omega_c}{\nu_B}$

$$D_\perp = \frac{1}{16} \frac{kT_e}{eB} = \frac{kT_e}{m_e} \frac{1}{\omega_c} \frac{\beta}{1 + \beta^2} \tag{2.52}$$

The problem with this method is that there are two limits for the maximum diffusion that can be achieved. The first one is set by the timestep: in one timestep, the electron velocity direction can be randomized only once, so $\nu_B^{max} < \frac{1}{\Delta t}$.

The second one is due to the solving of Eq. (2.52). the function $\frac{\beta_B}{1 + \beta_B^2}$ has a maximum: $\frac{1}{2}$ for $\beta_B = 1$.

These problems are explained in further detail in section 4.3, and a new implementation of the anomalous diffusion is described.

2.3.3   Implementation of the collisions

Collisions between two particle types are implemented in the code on a "particle" basis for the fast particle, and on a "fluid" basis for the slow one.

For example, for each electron in the electron loop, the code calculates the probability that this electron undergoes a collision event. Assuming the collisions are independent events, this is done by summing the ionization rates with the "slower" species, say 2:

$$\nu_{e2} = n_2 v_{e2} Q_{e2} \qquad (2.53)$$

where $v_{e2} = \|\vec{v}_e - \vec{v}_2^{bulk}\|$, $\vec{v}_2^{bulk}$ being the average velocity of the particles from species 2 interpolated at the electron location.

Assuming the collision events are independent, the probability that the electron undergoes one or more collisions can be shown to be

$$p = 1 - e^{-\nu \Delta t} \qquad (2.54)$$

where $\nu = \Sigma \nu_{ej}$ is the sum of all the different collision rates.

p has to be much less than one, to make sure that the probability that the electron collides more than once is negligible. Using a first order development of Eq. (2.54), that means $\frac{1}{\nu} << \Delta t$, and then $p \simeq \nu \Delta t$.

A random number then decides if a collision really happens, in which case the electron is modified by the event (this differs for the different events, and is explained in the following paragraphs), and the effect on population 2 is stored until the next loop moving that population.

Similarly, when looping through the ions, the collision events with neutrals are calculated, whereas the results of the collisions with electrons, from the electron loop, are applied.

Finally, as neutral-neutral collisions are neglected, collision results from ion and electron loops are applied to the neutrals when they are moved forward.

Collisions involving electrons

The electrons are the fastest species, hence any collision implying an electron is treated in the electron loop, as explained above.

- Elastic scattering

If an electron hits a neutral in an elastic scattering collision, the energy exchange, proportional to the reduced mass $\frac{m_e m_n}{m_e + m_n} \simeq m_e$, is negligible. Hence, the electron energy remains constant, but its velocity direction is randomized, while the neutral does not "see" any effect.

- Excitation

There are many levels of excitation for a Xenon atom. All these levels are lumped in the simulation in one single level at $8.32\,eV$ of energy, using data from Hayashi [9]. When an excitation event takes place, the electron energy is decreased by $8.32\,eV$, and its direction randomized. Most of the excited neutral radiates its energy immediately, therefore the effect on the neutral population is neglected. Still, it is possible that some excited atoms are long-lived (metastable), and those metastables may be easier to ionize than neutrals. This possibility should be investigated further.

- Neutral ionization

Two kinds of ionization are modeled: single and double ionization. An ion with single or double charge is created with the neutral bulk velocity, and the location of the neutral to delete, weighted on the grid nodes, is stored. A neutral at the appropriate location will be deleted during the next neutral loop. One or two electrons are created, with low energy. The initial electron has its velocity direction randomized, and its energy decreased by the created electron energy plus $12.1\,eV$ for a single ionization, or $32.0\,eV$ for a double ionization.

- Ion second ionization

A secondary electron is created, and the primary electron energy is decreased, as in the neutral ionization. The location of the double ionization is stored, and later when doing the ion loop, a single ion at the correct location will have its charge doubled.

Collisions involving ions

Collisions with electrons have been dealt with above, the collisions left are with neutrals.

- Charge exchange

  When a charge exchange occurs, the ion velocity is changed to the bulk neutral velocity interpolated at the ion location, a new neutral is created at the ion location, with the old ion velocity, and the collision location is stored: a neutral will be deleted in the next neutral loop.

- Scattering

  The ion velocity is calculated using a scattering event with an imaginary neutral of velocity equal to the neutral bulk velocity, interpolated at the ion location. The momentum change to be applied to that neutral is stored with its location for the next neutral loop.

2.4 Boundary conditions

The boundaries of the simulation include the free space boundaries and the walls. The wall boundary conditions are very important as they represent a big energy loss for the thruster, but they also affect the bulk plasma through the electric sheath properties.

2.4.1 Neutrals

Neutrals are injected at the physical location of the neutral injectors, with a half-Maxwellian distribution of $0.1\,eV$. They are bounced at walls with full accommodation, i.e. they are re-emitted with a half-Maxwellian distribution of temperature equal to the wall temperature, nominally 700K. The neutrals are free to leave the simulation region as no force or gradient pushes them back towards the thruster. When a particle leaves the simulation through a free space boundary, it is simply deleted.

2.4.2 Ions

Ions are created from ionization. They are "half-accommodated" at the walls as they are re-emitted as neutrals with a half-Maxwellian distribution of energy equal to half the incoming energy. Ions lose their charge at the wall because of recombination. They are free to leave at the free space: the electric field pushes them towards the exit, and no adverse gradient creates a positive flux inwards.

2.4.3 Electrons

Electrons are created physically at the cathode and in the bulk through ionization. The simulation does not include the cathode, still the free space boundary has to account for this injection. The solution adopted in the mini-TAL simulation is the free-space overall neutralization. The free space boundary being far away from the potential drop region where the plasma can be non-neutral, or from any wall sheath, we can assume that $n_e \simeq n_i$. Hence, by checking the total charge imbalance at that boundary, we can inject the number of electrons required to keep overall neutrality. These electrons are injected in the cells, according to their relative positive charges; they are given a thermal energy of $1\,eV$, along with a directed energy equal to the potential at that boundary, if the potential is higher than the cathode potential (0V). This model has been slightly modified, the modifications are presented in section 4.3.3

If the cells at the boundary are positively charged, no electrons are added, and neutrality should be reached because of the ion flux to the free space.

At the walls, electrons are removed, to account for the wall electron-ion recombination.

2.5 Artificial tricks

Now that we have looked at each of the physical parts of the simulation, we will focus on the three tricks used to make it faster: the superparticles, the artificial permittivity, and the artificial mass factor.

2.5.1 Superparticles

The number of electrons in the mini-TAL thruster can be roughly estimated from $n_e \simeq 5 \times 10^{12} \, cm^{-3}$ and $V \simeq 0.063 \, cm^3$; it is $N_e \simeq 3.15 \times 10^{11}$. The computational time of the leapfrog algorithm is proportional to the number of particles, and so is the memory required; such high particle numbers are above our computation capabilities.

Instead of modeling each single atom or electron, the code models "groups" of particles: superparticles. Any particle in the code stands for several millions of real particles. Nothing in the physics is changed; the code, instead of pushing and ionizing one million particles with very similar properties, deals with one. The only limit to that regrouping is the numerical noise due to a low number of particles per cell.

In order to avoid such artificial fluctuations, we need to keep the number of particles per cell high enough, especially in the most important part of the code: the ionization region. For each cell, we want a relative standard deviation

$$\sigma \propto \frac{1}{\sqrt{N}} << 1 \qquad (2.55)$$

For $N = 30$, $\sigma \simeq 0.18$. That means for the near-anode cells where the cell volume is on average $.05\pi \left(1.55^2 - 1.5^2\right) \simeq 0.023 \, mm^3$ and $n_e \simeq 1 \times 10^{13} \, cm^{-3}$, a superparticle size of 8 millions. With that superparticle size, near the exit of the thruster, at radius $1mm$, where $n_e \simeq 1 \times 10^{12} \, cm^{-3}$, and the cell volume is $.05\pi \left(1.55^2 - 1.5^2\right) \simeq 0.023 \, mm^3$, we have 8 particles per cell. Altogether, 41 000 particles are required.

A last refinement to that trick is the modular particle size: in the computation, $n_e \simeq n_i \simeq \frac{1}{10} n_n$. Hence, if the superparticles are sized to have at least 30 ions and electrons per cell, we will have 300 neutrals in the same cell, which is very cumbersome, especially as the code focuses on the charged particles. This is why neutrals are injected as superparticles with a numerical size 50 times higher than regular particles. Collision rates are determined by faster particles (see section 2.3.3), and deleting a neutral through ionization means decreasing the particle size by one, or deleting it if the size left is only one.

Charge exchange and ionization end up producing many particles of small size, hence a subroutine, *sweep()*, checks cells with too many neutral particles, and lumps

some of them until a more reasonable level is obtained.

2.5.2 Artificial permittivity

Debye length requirements

The electron temperature in the mini-TAL is of order $10\,eV$, and the average plasma density $n_e \simeq 5 \times 10^{12}\,cm^{-3}$, hence the Debye length in the mini-TAL is of order:

$$\lambda_d = \sqrt{\frac{\epsilon_0 k T_e}{e^2 n_e}} \simeq 10\mu m \tag{2.56}$$

The discretization of the Poisson equation in section 2.2 requires that the grid spacing be less than the Debye length. The characteristic length of the mini-TAL being a few mm, this would require a 500×500 grid, which the Poisson solver cannot handle: the computation time grows faster than the total number of cells.

The trick used to coarsen the grid requirements is an artificial permittivity. By replacing ϵ_0 by $\gamma^2 \epsilon_0$, with $\gamma = 10$, the Debye length becomes:

$$\lambda_d = \gamma \sqrt{\frac{\epsilon_0 k T_e}{e^2 n_e}} \simeq 0.1\,mm \tag{2.57}$$

This enables us to use the 87×49 grid of figure 2-6.

When adding this γ^2, energy, and therefore sheath magnitudes, are not changed as the formula for work of the electro-magnetic force $\int_{1\to2} \vec{E}d\vec{S} = -\int_{1\to2} \vec{\nabla}\phi d\vec{S} = \phi_2 - \phi_1$ is still valid.

However, the length-scale at which the phenomena takes place is increased. This creates a limit to the artificial permittivity factor that can be used: the Debye length has to remain much smaller than any dimension in the thruster, to keep the sheath size negligible.

Here, with $\gamma = 10$, the Debye length is of the order of $0.1\,mm$, when the distance between the anode and the wall is $0.5\,mm$, this means that we should expect some non-neutrality near the anode in the results. This has been observed.

43

Plasma time effects

The artificial permittivity also decreases the plasma frequency $\frac{1}{2\pi\gamma}\sqrt{\frac{e^2 n_e}{m_e \epsilon_0}} \simeq \frac{1}{\gamma} \times 2 \times 10^{10} Hz$. This is going to change the timestep required for the simulation, up to the limit of the Larmor motion time scale (section 2.2.4).

2.5.3 Artificial mass factor

Convergence time

The convergence of the PIC code is determined by the flight time of the slowest species: the neutrals and the ions.

Assuming the average ion velocity is $\frac{1}{2}$ of the exit velocity, and the acceleration efficiency $\frac{\frac{1}{2} m_{Xe} v_z^2}{e \Delta V} \simeq 0.75$,

$$< v_z > \simeq \sqrt{0.75 \frac{e \Delta V}{m_{Xe}}} \simeq 12,800 \frac{m}{s} \tag{2.58}$$

The timestep being of order $0.3\frac{\omega_c}{2\pi} \simeq 2.5 \times 10^{-12} s$, the axial length of the simulation region being of order $5\,mm$, the number of iterations required for an ion to leave the thruster is $160,000$.

Assuming the neutral axial energy is of order $0.5\,eV$, i.e. $< v_z > \simeq 560\frac{m}{s}$, the number of iterations for neutrals is 4×10^6.

A reasonable convergence time would be $100,000$ iterations. That means we need to increase the slow particle speed by a factor 40.

Increasing the slow species velocity

The velocity of the slow particles is increased, by artificially decreasing their mass:

$$m_{Xe}^{computation} = \frac{1}{mass\ factor} m_{Xe}^{real} \tag{2.59}$$

Typical values for the mass factor are $1,000$, or $2,500$. With these values, the mass ratio between electrons and neutrals/ions in the simulation remains large,

$$mass\ ratio = \frac{m_{Xe}^{computation}}{m_e} = \frac{1}{mass\ factor} \frac{2.2 \times 10^{-25} kg}{9.1 \times 10^{-31} kg} \tag{2.60}$$

96 for a mass factor of $2,500$; 242 for a mass factor of $1,000$.

Scaling due to the artificial mass ratio

Increasing the heavy particle velocities raises an obvious issue: if the mass flow remains constant, the neutral and the ion density are going to drop by the same factor by which the velocity increases. In order to preserve the densities, we need to increase the neutral mass flux by $\sqrt{\text{mass factor}}$, and figure out a way to increase the ionization rate. We will now have a look at the different physical sections of the code to see what needs to be modified:

- Poisson solver and leapfrog algorithm

  The only thing the Poisson solver takes into account is the charge density $\rho = -e\,(n_e - n_i)$. The densities being preserved (the trick to keep the ion density is explained in the "Collisions" part below), the Poisson solver is unaffected.

  The leapfrog algorithm (see section 2.2.3) first calculates the velocity at time t_{i+1}, integrating the equation of motion $\frac{m_{X_e}^{real}}{\text{mass factor}} \frac{d\vec{v}^{comp}}{dt} = \vec{F}_{E/M}^{real}$.

  The idea is to apply the same physical force to a particle $mass\,factor$ times lighter, in order to increase the velocity by $\sqrt{\text{mass factor}}$.

  In the neutral case, the electro-magnetic force is zero, nothing is changed. In the ion case, $F_{E/M}^{real} = e\left(\vec{E} + \vec{v}^{real} \times \vec{B}\right)$, where $\vec{v}^{real} = \frac{v^{comp}}{\sqrt{\text{mass factor}}}$. To preserve the electro-magnetic force, we need to modify the equation to integrate for the ions in replacing $\vec{v} \times \vec{B}$ by $\frac{\vec{v}}{\sqrt{\text{mass factor}}} \times \vec{B}$. The ions being non-magnetized, this is not very important in any case.

- Collisions

  Collisions, governed by a collision rate of the form $\nu_{12} = n_2 v_{12} Q_{12}$ include velocity-dependency in the v_{12} and in the $Q_{12}\,(\nu_{12})$ terms.

  The ionization rate for single ionization, neglecting v_i compared to v_e, is:

  $$R_i = n_e n_i v_e Q\,(v_e) \tag{2.61}$$

  As we are conserving densities, and v_e is unaffected by the mass factor, this formula, and similarly the formula for double ionizations, are unchanged by the

45

mass factor. As explained above, we need to increase these ionization cross-sections by a factor $\sqrt{\text{mass factor}}$ to catch up with the higher neutral flux.

Other electron-neutral and electron-ion cross sections must also be increased by $\sqrt{\text{mass factor}}$. This higher-than-normal rates compensate for the shorter flight time of neutrals and ions. This means in turn that the electron population undergoes many more events that they should (the ratio being, again, $\sqrt{\text{mass factor}}$). To keep the electron flux scaling, we need in turn to increase the diffusion by the same ratio. It is indeed not possible to increase ionization without letting the cross-field transport increase by the same ratio.

Ion-ion, and ion-neutral collisions are governed by a rate of the form:

$$R = n_n n_i v_{ni} Q\left(v_{ni}\right) \quad \text{neutral-ion example} \tag{2.62}$$

Here, the computational v_{ni} is too high by $\sqrt{\text{mass factor}}$. Hence, we need to multiply it by $\sqrt{\frac{1}{\text{mass factor}}}$ before using it to calculate the cross-section $Q\left(v_{ni}\right)$. For the same reduced time-of-flight argument, the collision rate has to be higher-than-normal by $\sqrt{\text{mass factor}}$. The higher velocity v_{ni} in (2.62) outside the cross-section formula will increase this rate naturally.

- Boundary conditions

Here we will list the different kinds of boundary conditions and see how they are affected by the mass ratio.

The right-hand-side free space boundary is unchanged: more ions are leaving but the neutrality condition injects more electrons if and where necessary.

The floating walls receive more ions: according to the classical sheath theory, ion flux to the wall is

$$j = e n_i \sqrt{\frac{kT_e}{m_i}} \exp\left(-\frac{1}{2}\right) \tag{2.63}$$

where m_i is now lower. As sheaths in the PIC code are self-consistently built, the electron flux to the wall will adjust and be higher-than-normal by a factor

$\sqrt{\text{mass factor}}$. One issue appears: the sheath adapts to let more electrons in, by decreasing its voltage drop magnitude. The number, and charge flux is correct, but the energy flux is now wrong: because of the weak sheath, the electrons that can make it to the wall can be low-energy electrons. A fix for that has been developed and is explained in section 4.3.2.

The flux to fixed-potential boundaries such as the anode is limited by the number of electrons available next to the anode: by the electron flux upstream in the chamber for the anode for example. The ionization rate, and the cross-field diffusion being higher by $\sqrt{\text{mass factor}}$, the flux to the wall is higher by the same factor.

2.5.4   How to scale everything

The units to be scaled are number of particles, time, length, and electric potential. Any other unit is a combination of these units and as such its scaling can be calculated as a function of these 4 units.

- Number of particles

  Computational electrons or ions are superparticles, as explained in section 2.5.1. Neutrals are multiple superparticles: they have a variable weight> 1, stored with the particle properties equal to the number of superparticles they represent. This means that when calculating the densities, one has to account for the superparticle size and the variable weight (for neutrals). Other than that, collisions, leaping forward or boundary conditions are not modified.

- Time

  We introduced two factors that change the timescale. First, the artificial permittivity changes the plasma time scale; second, the mass factor changes the mass of the heavy particles, which has the same effect as changing the timescale for them and keeping the correct particle weight, as far as the equation of motion

is concerned:

$$\frac{m_{Xe}}{\text{mass factor}}\frac{d\vec{v}}{dt} = m_{Xe}\frac{d^2\vec{x}}{d\left(\sqrt{\text{mass factor}}\,t\right)^2} \tag{2.64}$$

that assumption is valid as long as the force on the right-hand side is independent of time, which is not true for ions, but that has been taken into account in section 2.5.3 by adjusting the velocity in the $\vec{v} \times \vec{B}$ term.

So, any effect involving the electrons happens on the correct timescale, except plasma oscillations, happening γ times too fast.

However, phenomena involving ions or neutrals happen $\sqrt{\text{mass factor}}$ per species involved too fast. Ionization oscillations for instance, using a predator-prey model, have a frequency of

$$\Omega = \frac{1}{2\pi}\frac{\sqrt{V_i V_n}}{L} \tag{2.65}$$

where L is the length scale at which the ionization happens, and V_i and V_n are the *real* ion and neutral velocities. When using the $\sqrt{\text{mass factor}}$ coefficient, Eq. (2.65) becomes:

$$\Omega^{real} = \frac{1}{2\pi}\frac{\sqrt{V_i^{computational}V_n^{computational}}}{L\,\text{mass factor}} \tag{2.66}$$

Hence, the computed oscillation frequency is expected to be mass factor larger than observed in the real plasma.

- Length

  The artificial permittivity modifies the length at which plasma shielding phenomena take place: it is increased by a factor of γ. Other lengths should not be affected, for instance the ionization scale.

- Electric potential

  Similarly to Eq. (2.64), the equation for the potential can be written as:

$$\frac{d^2\phi}{d\left(\frac{x}{\gamma}\right)^2} = \frac{\rho}{\epsilon_0} \tag{2.67}$$

  Hence, the electro-magnetic part of the code is unchanged, except for its length scale.

Chapter 3

Results at high voltage

This chapter presents PIC results for the modified mini-TAL 50W thruster at high voltage. It is based on results presented in [4] Results at low voltage of both modified and non-modified thrusters by Szabo are presented in [23].

The results, summarized in Table 3.2, and Figures 3-1 to 3-11, are for

- superparticle= 2.8×10^6 particles

- $\gamma = 10$

- mass factor= 2500

A case with such parameters takes about $80,000$ iterations to converge, but, starting from a converged solution and modifying slightly the parameters enable convergence in only $20,000$ iterations.

Section 3.1 presents a summary of the aggregate results and their trends, plus a comparison of the 2-D distributions (plasma density, electric potential, temperature, ionization rate) at two different voltages.

Section 3.2 contains more detailed analysis and discussions of some of the salient trends found. Section 3.2.1 illustrates changes vs. mass flow rate at fixed voltage. Section 3.2.2 (and Appendix A) breaks the efficiency down to its various components, and discusses their individual trends vs. voltage.
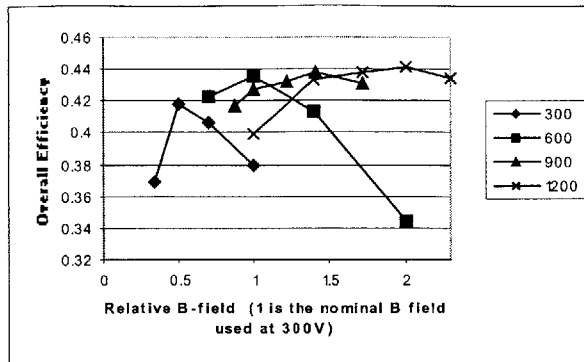
Figure 3-1: Efficiency at different B-fields for different voltages

3.1 Performance results

3.1.1 Global performance parameters

The main parameters characterizing the thruster's operation at a variety of conditions are collected together in Table 3.2. Except for one case at $V = 600V$, the rest are all at the normal flow rate. At each voltage the magnetic field was optimized (coarsely) with respect to overall efficiency; for $600V$, the nominal B field was found to be approximately optimal. The results of [13] suggest that B_{opt} scales as $\sqrt{V}$ for SPT-type thrusters, and there is some theoretical justification for this scaling, in that this would preserve the Larmor radius of electrons with speeds proportional to $\sqrt{V}$. Our results (Fig. 3-1) seem to depart from this law towards $B \sim V$, which is the behavior found theoretically in [1] to describe the upper limit of the existence domain for steady flow solutions in a TAL-type of thruster (no strong wall losses).

Table 3.2 indicates that the various computed currents stay fairly constant as V is varied, except for some noticeable increase in the anode (or cathode) current between $300V$ and $600V$.

The mass flow is broken down in Table 3.2 into its constituents as they leave the engine: simple ions, double ions and neutrals. The most interesting part of these results is the double ion fraction. This is extracted into Table 3.1.1, together with the results for thrust contributed by the various species.

50

V (Volts)	300	600	900	1200
$\frac{\dot{m}^{++}}{\dot{m}^{+}}$	0.088	0.123	0.145	0.168
$\frac{I_b^{++}}{I_b^{+}}$	0.202	0.247	0.271	0.303
$\frac{F^{++}}{F^{+}}$	0.149	0.178	0.196	0.218

Table 3.1: Computed contributions of double ions to mass flow, beam current and thrust (for 0.1 mg/s)
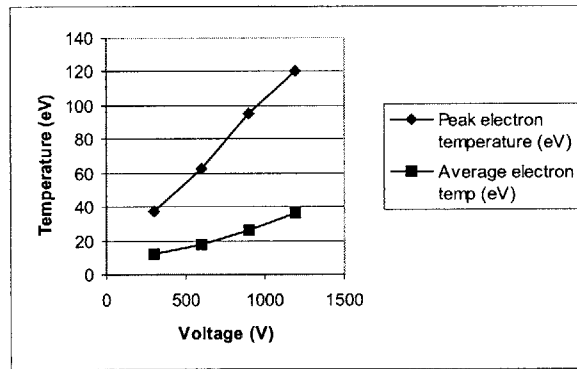
Figure 3-2: Peak and average electron temperature for different voltages, at optimum B-fields

More will be said about these results in Sec. 3.2, but it is worth pointing out at this time that the various double ion contributions increase strongly with voltage only at the low end of the range, and tend to saturate to nearly constant values at the higher voltages.

The thrust and specific impulse increase roughly as $\sqrt{V}$, as expected. The mean electron temperature ($< T_e >$, in eV) is shown in the next line of Table 3.2, and also in Fig. 3-2. The variation with voltage approaches proportionality at high V, but is slower than that initially. This may imply reductions of beam divergence between $V = 300V$ and, say, $600V$, because the radial ion thermal speed will increase less rapidly than their axial speed, but our computation cannot accurately extend out to the plume to verify this.

The potential of the outer channel wall is computed assuming the wall is metallic and electrically floating. Table 3.2 shows that this wall remains very close to cathode

potential throughout. This is in accordance with TAL experimental evidence and is probably due to the fact that some magnetic lines from the cathode region intercept that wall (Fig. 2-6).

The particle number densities at a selected point are also indicated in Table 3.2. There is some randomness in these "typical" results, due to motion of the ionization region with respect to the chosen point, but we can observe a general trend for ion densities to decrease with voltage, presumably as a consequence of their higher speeds (and despite somewhat increased ionization fractions). The neutral density falls faster, since both effects add together for them.

A similar message is conveyed by the total mass of neutrals and ions in the simulation, also reported in the table.

The last section of Table 3.2 concerns the various pieces that go into the calculation of overall efficiency, defined as $\eta = \frac{T^2}{2\dot{m}I_a\Delta V}$. We will here only comment on the overall efficiency itself (last line in Table 3.2), and leave a more detailed discussion for Sec. 3.2. If we compare the cases run at "nominal B field" (Fig. 3-3), we can see a clear optimum at $V = 600V$ ($\eta = 0.419$), with a rapid rise from 300 to 600V and a slower decrease beyond 600V. The comparison at near-optimum B field (Fig. 3-4) still shows a monotonic increase of efficiency with voltage, although with a noticeable weakening of the trend between 600 and 900V. This is similar to the experimental data of [3]. In [17] (single stage case), there is actually a small decreases in efficiency in the intermediate range, followed by increases at higher voltages. [10] and [13] show distinct optima near 600V.

3.1.2 Spatial Distributions at two Voltages

For the voltages of 300V and 600V, at nominal B-field, Figs. 3-5 through 3-11 summarize the time-averaged results for the main plasma quantities of interest.

Fig. 3-5 refers to electron temperature (ignoring the differences between $T_\perp$ and $T_\parallel$ which were reported in [24]- [22]). At 300V, T_e is about $4\,eV$ near the cathode and inside the anode channel, and reaches about $40\,eV$ in the region of the anode opening. A secondary maximum of T_e can be seen along the thruster axis, where an
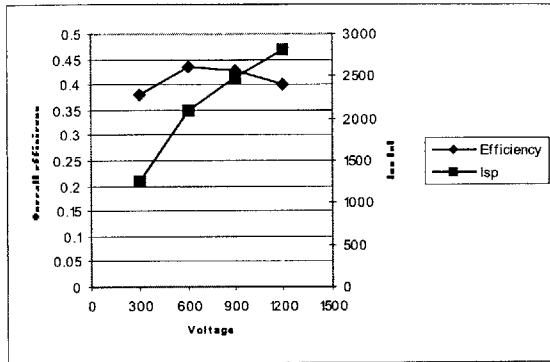
52

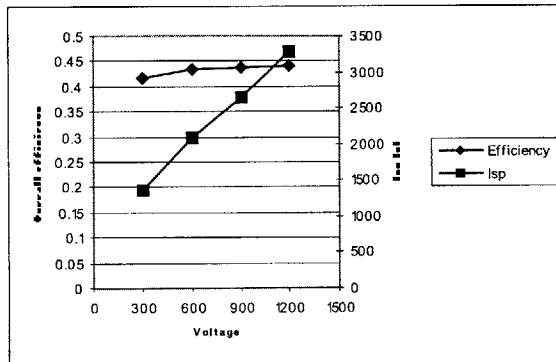Figure 3-3: Efficiency and Specific Impulse versus Voltage at constant B-field

Figure 3-4: Efficiency and Specific Impulse versus Voltage at optimum B-field

intensely luminous "spike" is normally observed. For $600V$, the peak temperatures reach $60\,eV$.

The potential maps (Fig. 3-6) are fairly similar in shape in both cases.The high field, or acceleration region, extends only about the width of the anode downstream, and fairly low potentials are seen beyond this point. However, the spike region, near the axis, also shows increased potentials, in both cases to about $40\,eV$.

The electron densities are mapped in Fig. 3-7. The most interesting observation is that the highest density is actually in the spike region, where it reaches about $8 \times 10^{19} m^{-3}$. This accounts for the strong luminosity of this region, which, however, is small in volume, as it lies so close to the axis. Its origin is mainly kinematical, a result of the crossing of many ion trajectories from all around the anode annulus. The principal plasma region is a ring in front of the anode, where n_e peaks at about $1.6 \times 10^{19} m^{-3}$ for $300V$, and about $1.3 \times 10^{19} m^{-3}$ for $600V$.

Figures 3-8 to 3-10 detail the various ionization processes. In Fig. 3-8, the first ion production is seen to peak in the main plasma ring near the anode, where both n_e and n_n as well as T_e are high. The peak value is lower at $600V$ than at $300V$, reflecting the lower n_e and n_n principally. Fig. 3-9 shows production of double ions from neutrals following $n + e^- \rightarrow i^{++} + 3e^-$. This process occurs fairly much concurrently with single-ion formation, since the same ingredients feed into both. Once again, the maximum rate is lower at the higher voltage.

By contrast, Fig. 3-10 shows that those double ions which originate from single ions by $i^+ + e^- \rightarrow i^{++} + 2e^-$ do so predominantly in the spike region. This is because of the very high first ion density in this region, while neutrals, absent there, are not involved. Altogether, both double ion production channels contribute about equally to the total, but their very different geometrical distribution has interesting and strong consequences, to be expanded upon in Sec. 3.2. We only advance here the observation that double ions from the second channel (Fig. 3-10) are created at very low potentials, and contribute little to thrust.

Finally, Fig. 3-11 details the rate for the one lumped neutral excited level population rate. It is assumed in the code that the corresponding excitation energy is
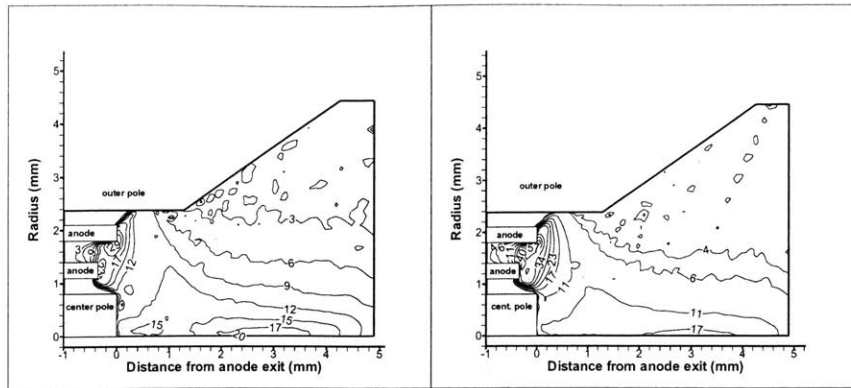
Figure 3-5: Electron temperature in eV, voltages 300 and 600V
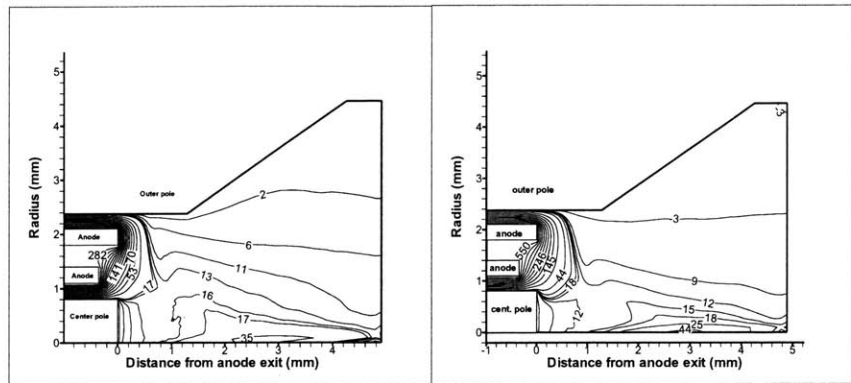
Figure 3-6: Potential in V, voltages 300 and 600V

fully lost by prompt radiative decay. As expected, this process is fairly similar in distribution to ionization, and, once again, it is seen to decrease in intensity as voltage increases.

3.2 Trends

3.2.1 Effects of mass flow changes

Table 3.2 contains two cases for $V = 600V$, $B = B_{NOMINAL}$, one of which has $\dot{m} = 0.1052mg/s$ (nominally $0.1mg/s$), while the other has $0.1875mg/s$ (nominally $0.167mg/s$). Because of the increased collisionality, one might expect the case with
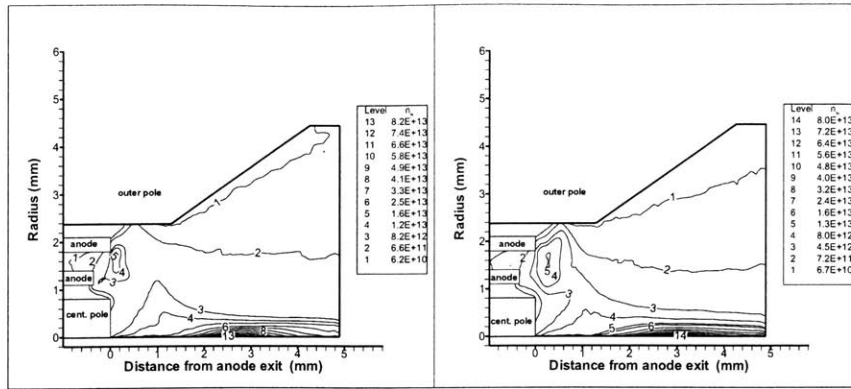
Figure 3-7: Electron density in cm^{-3}, voltages 300 and 600V
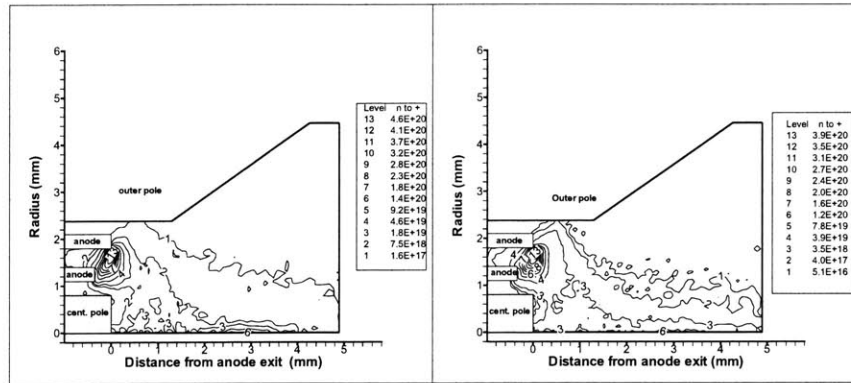
Figure 3-8: Single ion creation from neutrals per unit volume in $cm^{-3}s^{-1}$, voltages 300 and 600V
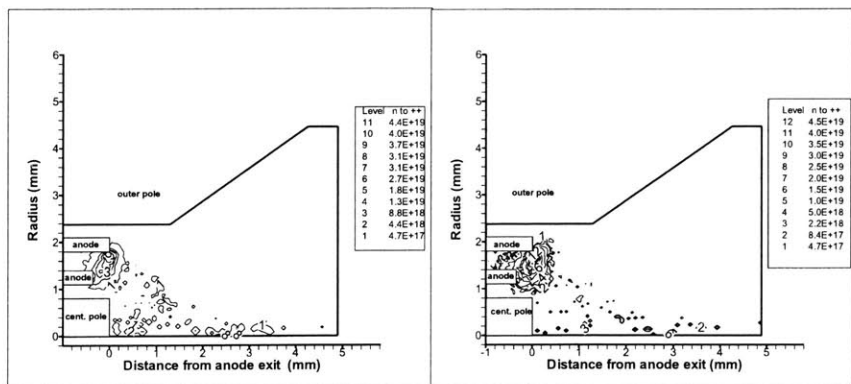
Figure 3-9: Double ion creation from neutrals per unit volume in $cm^{-3}s^{-1}$, voltages 300 and 600V

56
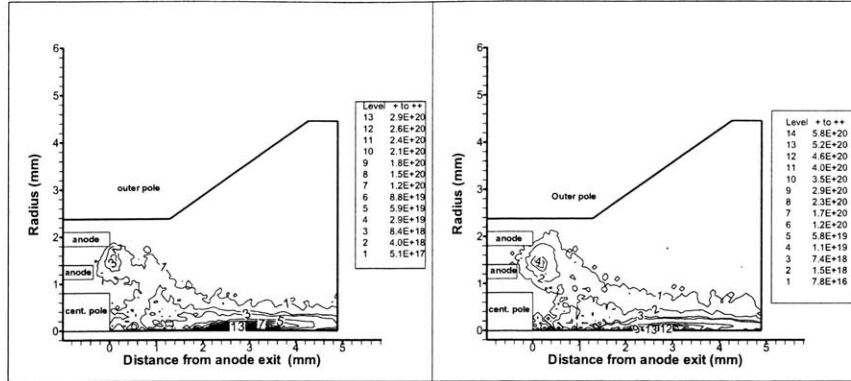
Figure 3-10: Double ion creation from single ion per unit volume in $cm^{-3}s^{-1}$, voltages 300 and 600V
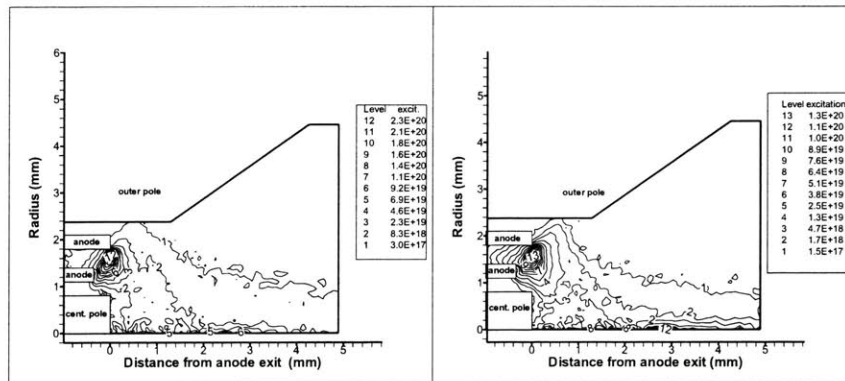
Figure 3-11: Neutral excitation per unit volume per unit volume in $cm^{-3}s^{-1}$, voltages 300 and 600V

higher flow to show lower electron temperature and perhaps also lower double-ion fractions. Examination of the results in Table 3.1.1 shows in fact the opposite trends. This can be explained as follows: since n_e increases with $\dot{m}$, the mean free path of a given neutral between ionizing collisions decreases, and neutrals are more likely to be ionized. This is borne out in the result by the larger ratio of total mass of ions to total mass of neutrals for the higher $\dot{m}$, as well as by the densities at the central point. This then means that a given electron will collide with fewer neutrals, and will experience lower ionization and excitation energy losses. Since the energy source (the potential difference) has not changed, a higher electron temperature will result.

Regarding double ions, the ratio of their production rate to that of first ions is

$$\frac{\dot{n}^{++}}{\dot{n}^{+}} = \frac{k_{02}\left(T_e\right)n_n n_e + k_{12}\left(T_e\right)n^+ n_e}{k_{01}\left(T_e\right)n_n n_e} \tag{3.1}$$

$$= \frac{k_{02}\left(T_e\right)}{k_{01}\left(T_e\right)} + \frac{k_{12}\left(T_e\right)n^+}{k_{01}\left(T_e\right)n_n} \tag{3.2}$$

The small change in T_e is not a strong effect, since most electrons are well above threshold for these transitions at the prevalent high temperatures. The factor $\frac{n^+}{n_n}$ in the second term indicates therefore that there will be proportionally more double ions produced from first ions when $\dot{m}$ increases. Since the other production channel (from neutrals) will change little, we can expect an increased double ion fraction at higher flow, as indeed the table shows: 12.4% double ion mass flow fraction at $0.1 mg/s$, vs. 18.1% at $0.167 mg/s$. The other conclusion from Eq. (3.1) is that, because the double ions formed from first ions are mainly produced in the low-potential spike region, the mean velocity of double ions will be reduced as $\dot{m}$ increases. This is confirmed by the $\beta^{++} = \frac{v_z^{++}}{v_z^+}$ factors also listed in Table 3.2: 1.32 for the low-flow case, vs. 1.22 for the higher flow case (recall that β^{++} would be $\sqrt{2} \simeq 1.414$ if double ions were created in the same region as single ions).

Finally, in terms of performance, there is a significant increase in specific impulse (Isp) and a small increase in efficiency at the higher flow rate. The higher Isp results from the higher proportion of the flow, which is in the form of ions, and especially of double ions. The higher efficiency is driven by the larger value of $\eta_e = \frac{I_b}{I_a}$, which in turn appears to result from the fact that many of the secondary electrons produced in

the low-potential region by the process $i^+ + e^- \rightarrow i^{++} + 2e^-$ actually pass downstream into the beam instead of back-streaming to the anode.

3.2.2 Analysis of Efficiency Changes vs Voltage

The introduction of second ionization in the simulation necessitates some redefinition of the familiar fractional efficiencies used for Hall thrusters. This is summarized in our Appendix A. In short, the overall (anode) efficiency is the product of four factors:

1. the "Dispersion Efficiency", which penalizes non-axial first ion discharge,

2. the "Acceleration Efficiency", which represents the ratio of the mean potential at which first ions appear to the applied voltage,

3. the "Electrical Efficiency", or ratio of beam to anode or cathode current, and

4. the "Effective Utilization Efficiency", which in the absence of double ions would reduce to the fraction of mass flowing out as ions; the double ions introduce a correction factor for this, which depends on the ratio of mean velocity of double ions to that of the single ions, and which is greater than unity.

Upon examination of the relevant part of Table 3.2 (the last block of rows), the first striking piece of information is the value of the Electrical Efficiency, which remains in the neighborhood of unity, even higher in some cases. This means that the beam current is comparable to or larger than the anode current, which is not a familiar situation (values of 0.6-0.7 are common for this ratio). The implication is that a good number of secondary electrons from ionization events manage to leave with the ions and help neutralize the beam, without having to back-stream to the anode and be re-injected as cathode current. We have verified that this is indeed what the computation shows, and the inference is that this effect is due to the high rate of second ion creation from first ions in the spike region (Fig. 3-10), at potentials below about 30 Volts (Fig. 3-6). Whether this is peculiar to this thruster's geometry (small ratio of inner to outer annulus ratio, which would tend to enhance the spike effect) needs to be resolved in future. Aside from the unexpected magnitude of this ratio,

its trends are intelligible. For instance, if B is kept constant, the beam/anode current ratio decreases as voltage is raised. This indicates that electron back-streaming is being facilitated by the higher anode potentials. On the other hand, if we compare the B-field optimized cases, the ratio remains about constant, as the additional impedance keeps back-streaming in check.

Regarding the utilization efficiency (either for single ions or the corrected "effective" value), we can see in Table 3.2 that, both at constant B and for the B-optimized cases, the trend is to rise fairly rapidly between 300 and $600V$, then to saturate at nearly constant values. This may be related to the increase of the electron temperature with voltage, which makes a strong impact on ionization at the lower end of the voltage range. At low T_e, a temperature increase moves more electrons into the high cross-section range; at the higher temperatures, most electrons are beyond the ionization threshold, and are in fact moving into the decreasing part of the cross-section curve. For related reasons, we have noticed that the excitation/radiation losses become a smaller fraction of the total electron energy balance at higher voltages.

As noted, total (single+double) ion utilization efficiency rises steadily from under 80% to more than 90% as applied voltage is increased from $300V$ to $1.2kV$. The average degree of gas ionization remains at about 4%, with a slight tendency to decrease. This indicates that the ion velocity is increasing faster than the neutral velocity, and so we can conclude that charge-exchange is not an important factor overall.

Interestingly enough, the degree of xenon ionization at the chosen fixed point in the anode layer changes drastically from 7% to 55% as the anode potential rises, while plasma and gas densities drop by factors 2 and 20, respectively. This shows that the ionization front is penetrating closer to the anode as the voltage increases, so the test point is in the highly ionized region at high voltages.

In connection with this, we can examine the behavior of the Acceleration Efficiency. At constant B-field, and at least above $600V$, this quantity decreases with voltage, probably because ionization begins whenever electrons have gathered enough energy, and this happens at a lower fraction of the total potential when this potential

is high. In contrast, for the B-optimized cases the acceleration efficiency increases in the same voltage range; this appears to be consistent with our earlier observation that the ionization layer is moving closer to the anode, and hence to the anode potential, in those cases.

Because ion utilization efficiency stays high, the plasma production rate (if neutral wall recycling is low) has to be about the same:

$$\int N \frac{\int Q_i f_e d^3v}{\int f_e d^3v} \sqrt{T_e} n_e d^3r \simeq const. \tag{3.3}$$

From Fig. 3-2 one can see that the electron temperature, T_e, goes up by a factor of 3. As i) the electron temperature is always above ionization potential (12 eV), ii) the electron impact ionization cross-section saturates and even goes back at higher energies (see relevant data in [22]), and iii) PIC simulations [24], [23] show that the electron distribution function (EDF) is close to Maxwellian, we may assume that the effective propellant ionization rate, $\frac{\int Q_i f_e d^3v}{\int f_e d^3v} \simeq const.$ as well. Thus the expression under the integral in Eq. (3.3) is reduced by an order of magnitude in our range of voltages. The only possibility to compensate for that is to increase the area of integration (i.e., with substantial ionization) by the same factor. This tendency can be seen from Fig. 3-8, and 3-11, where contours of electron impact excitation are shown. The expansion of the layer can be seen from Fig. 3-7 as well.

The Dispersion Efficiency (reflecting the single ion exit angles) has an interesting and not fully understood behavior. For constant B, it increases slightly with voltage, apparently reflecting a slower-than-proportional increase of electron temperature with voltage. But at optimum B, the trend is clearly reversed. Further analysis of this and of its relationship to beam divergence is needed.

All these results appear to validate the usefulness of this numerical tool for identifying detailed trends and effects. Among the important results of this work, we can mention:

- The calculation of the optimum magnetic field at each voltage

- The existence of a maximum efficiency if the magnetic field is not optimized

61

- The disappearance (or near disappearance) of this maximum when the magnetic field is optimized

- The nearly linear increase of electron temperature with voltage

- The spatial separation of the two channels for double ion formation, with one of them predominating in the low-potential central spike

- The identification of most of the detailed mechanisms for efficiency variation, through a detailed analysis of its constitutive factors

After looking at TAL thrusters, we re now going to investigate a 3kW class SPT thrusters, in chapter 4.

Table 3.2 (page 63)

			300	**300**	300	300	600	**600**	600	600	900	900	900	**900**	900	1200	1200	1200	**1200**	1200	600
Mass flow (mg/s)			0.1	**0.1**	0.1	0.1	0.1	**0.1**	0.1	0.1	0.1	0.1	0.1	**0.1**	0.1	0.1	0.1	0.1	**0.1**	0.1	0.167
B field (relative to nominal)			0.35	**0.5**	0.7	1	0.7	**1**	1.4	2	0.87	1	1.22	**1.41**	1.72	1	1.4	1.72	**2**	2.3	1
Currents (A)																					
	cathode		0.0732	**0.0693**	0.0677	0.0651	0.0744	**0.0766**	0.0823	0.0782	0.0803	0.0768	0.0790	**0.0826**	0.0802	0.0800	0.0789	0.0797	**0.0810**	0.0826	0.1348
	anode		0.0737	**0.0693**	0.0676	0.0649	0.0742	**0.0771**	0.0818	0.0782	0.0804	0.0770	0.0787	**0.0826**	0.0802	0.0804	0.0791	0.0789	**0.0802**	0.0831	0.1330
	beam		0.0599	**0.0647**	0.0663	0.0670	0.0707	**0.0773**	0.0846	0.0837	0.0765	0.0752	0.0789	**0.0824**	0.0835	0.0747	0.0779	0.0807	**0.0835**	0.0850	0.1500
	ionization		0.0793	**0.0747**	0.0764	0.0803	0.0765	**0.0829**	0.0896	0.0892	0.0817	0.0792	0.0826	**0.0871**	0.0853	0.0811	0.0821	0.0836	**0.0849**	0.0887	0.1551
Mass flows (mg/s)																					
	neutrals		0.0221	**0.0218**	0.0222	0.0221	0.0121	**0.0128**	0.0106	0.0118	0.0104	0.0101	0.0092	**0.0078**	0.0072	0.0097	0.0080	0.0074	**0.0059**	0.0049	0.0171
	ions	total	0.0737	**0.0792**	0.0805	0.0799	0.0860	**0.0924**	0.0983	0.0957	0.0925	0.0907	0.0939	**0.0971**	0.0971	0.0903	0.0925	0.0945	**0.0965**	0.0969	0.1704
		single	0.0659	**0.0703**	0.0706	0.0685	0.0755	**0.0794**	0.0813	0.0774	0.0809	0.0790	0.0804	**0.0819**	0.0805	0.0788	0.0789	0.0790	**0.0792**	0.0780	0.1365
		double	0.0079	**0.0089**	0.0098	0.0114	0.0104	**0.0130**	0.0170	0.0184	0.0116	0.0117	0.0135	**0.0152**	0.0167	0.0115	0.0136	0.0155	**0.0172**	0.0189	0.0340
Thrust (mN)																					
		total	1.190	**1.274**	1.255	1.185	1.877	**2.013**	2.078	1.840	2.440	2.395	2.484	**2.586**	2.529	2.719	2.840	2.900	**2.949**	2.948	3.612
	ions	single	1.017	**1.084**	1.058	0.978	1.577	**1.655**	1.642	1.418	2.040	1.994	2.029	**2.080**	1.996	2.268	2.311	2.310	**2.305**	2.252	2.773
		double	0.173	**0.190**	0.197	0.207	0.300	**0.358**	0.436	0.422	0.401	0.401	0.454	**0.506**	0.533	0.451	0.529	0.590	**0.643**	0.696	0.839
	neutrals		0.057	**0.052**	0.048	0.045	0.048	**0.038**	0.029	0.028	0.052	0.046	0.342	**0.027**	0.021	0.051	0.034	0.275	**0.019**	0.014	0.063
Isp (s)			1276	**1356**	1328	1252	1961	**2087**	2141	1903	2536	2483	2567	**2659**	2600	2822	2928	2982	**3023**	3023	2255
Average electron temp (eV)			13.5	**12.0**	11.4	12.1	17.8	**17.8**	19.6	21.8	24.9	24.7	25.2	**26.6**	28.5	32.5	33.1	34.6	**36.7**	37.9	19.2
Phi wall (V)			0.03	**0.00**	0.00	-0.01	-0.01	**-0.13**	-0.25	-0.31	0.00	-0.05	-0.15	**-0.23**	-0.41	0.00	-0.16	-0.32	**-0.55**	-0.88	-0.02
Densities in ioniz. region (cm-3)																					
	+ charges		2.66E+12	3.12E+12	3.32E+12	3.42E+12	2.62E+12	2.89E+12	2.66E+12	2.15E+12	2.40E+12	2.72E+12	2.47E+12	2.32E+12	1.88E+12	2.18E+12	2.03E+12	1.87E+12	1.59E+12	1.50E+12	3.64E+12
	neutrals		4.51E+13	3.92E+13	4.06E+13	3.73E+13	3.18E+13	1.57E+13	6.60E+12	3.91E+12	2.81E+13	2.04E+13	7.96E+12	4.43E+12	1.28E+12	2.43E+13	5.55E+12	1.54E+12	8.90E+11	9.46E+10	1.49E+13
Total mass (mg)																					
	ions		3.78E-08	3.99E-08	4.21E-08	4.55E-08	2.95E-08	3.04E-08	3.09E-08	3.29E-08	2.58E-08	2.48E-08	2.48E-08	2.41E-08	2.27E-08	8.36E-07	2.08E-08	2.02E-08	1.91E-08	1.86E-08	5.40E-08
	neutrals		1.02E-06	1.02E-06	1.04E-06	1.06E-06	8.85E-07	8.70E-07	8.27E-07	8.36E-07	8.46E-07	8.51E-07	8.29E-07	8.08E-07	7.91E-07	2.21E-08	8.05E-07	7.85E-07	7.70E-07	7.61E-07	1.28E-06
Efficiencies																					
	electrical		0.818	**0.933**	0.979	1.03	0.951	**1.01**	1.03	1.07	0.952	0.978	0.998	**0.998**	1.04	0.935	0.987	1.01	**1.03**	1.03	1.11
	single ions	utilization	0.687	**0.695**	0.688	0.671	0.77	**0.755**	0.746	0.719	0.786	0.784	0.78	**0.781**	0.771	0.788	0.785	0.776	**0.774**	0.766	0.728
		acceler.	0.629	**0.629**	0.597	0.549	0.576	**0.583**	0.568	0.488	0.561	0.565	0.571	**0.584**	0.574	0.55	0.576	0.584	**0.592**	0.591	0.572
		dispersion	0.86	**0.859**	0.852	0.842	0.857	**0.846**	0.816	0.78	0.855	0.852	0.844	**0.835**	0.81	0.855	0.844	0.828	**0.81**	0.801	0.818
	double ions	utilization	0.0822	**0.0885**	0.0958	0.112	0.106	**0.124**	0.156	0.171	0.113	0.116	0.131	**0.145**	0.16	0.115	0.135	0.152	**0.168**	0.186	0.181
		beta	1.42	**1.37**	1.34	1.27	1.38	**1.32**	1.27	1.25	1.37	1.36	1.33	**1.31**	1.29	1.36	1.33	1.31	**1.28**	1.27	1.22
	neutrals	utilization	0.2308	**0.2165**	0.2162	0.217	0.124	**0.121**	0.098	0.11	0.104	0.1	0.089	**0.074**	0.069	0.097	0.08	0.072	**0.058**	0.048	0.091
		beta	0.167	**0.155**	0.145	0.144	0.191	**0.143**	0.135	0.131	0.199	0.181	0.147	**0.139**	0.115	0.181	0.147	0.128	**0.114**	0.101	0.182
	effective utilization		0.8332	**0.8282**	0.817	0.7968	0.8997	**0.8734**	0.8663	0.8455	0.9135	0.9068	0.898	**0.899**	0.8899	0.909	0.9035	0.8971	**0.8931**	0.8912	0.855
	Overall		0.3687	**0.4175**	0.4068	0.3794	0.4224	**0.4351**	0.4136	0.3444	0.4171	0.4269	0.4319	**0.4375**	0.4303	0.3997	0.4335	0.4382	**0.4411**	0.4345	0.4441

Table 3.2: PIC computation results for the mini-TAL at different voltages, magnetic fields and mass flow

Chapter 4

P5 thruster

4.1 The P5 thruster

The P5 thruster is a 3kw SPT-type thruster developed by Frank Gulczinski at University of Michigan [7]. Applied voltage is 300V, current 10A, and mass flow $11.50\,mg/s$. The geometric configuration and the magnetic field are shown in Figs. 4-1 and 4-2. Detailed design can be found in [7].

This thruster is about 20 times longer than the mini-TAL, but due to its high-average-radius chamber, its volume is 5800 times higher at $448\,cm^3$. Wall surface in contact with the plasma is 420 times larger at $325\,cm^2$.

The reasoning scheme to scale the different parameters in the code is the same as for the mini-TAL by James Szabo, and is summarized in Fig. 4-4. It is developed in sections 4.1.1 to 4.1.4.

With densities down one order of magnitude from the mini-TAL (Fig. 4-3), the collision phenomena to include in the model are the same, only charge-exchange is likely to be more important, due to the larger size of the thruster.

4.1.1 Gridding

The plasma in the chamber is less dense than in the mini-TAL, as shown on Fig. 4-3, and a bit cooler; the Debye length is of order $0.02\,mm$, higher than the $0.006\,mm$ of
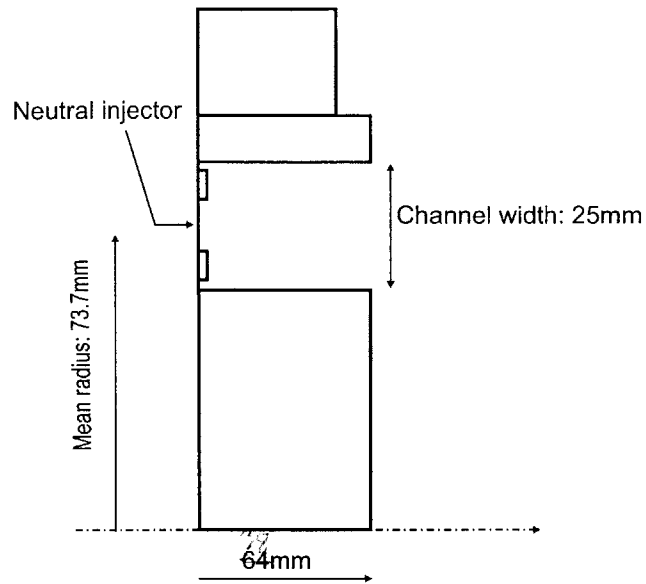
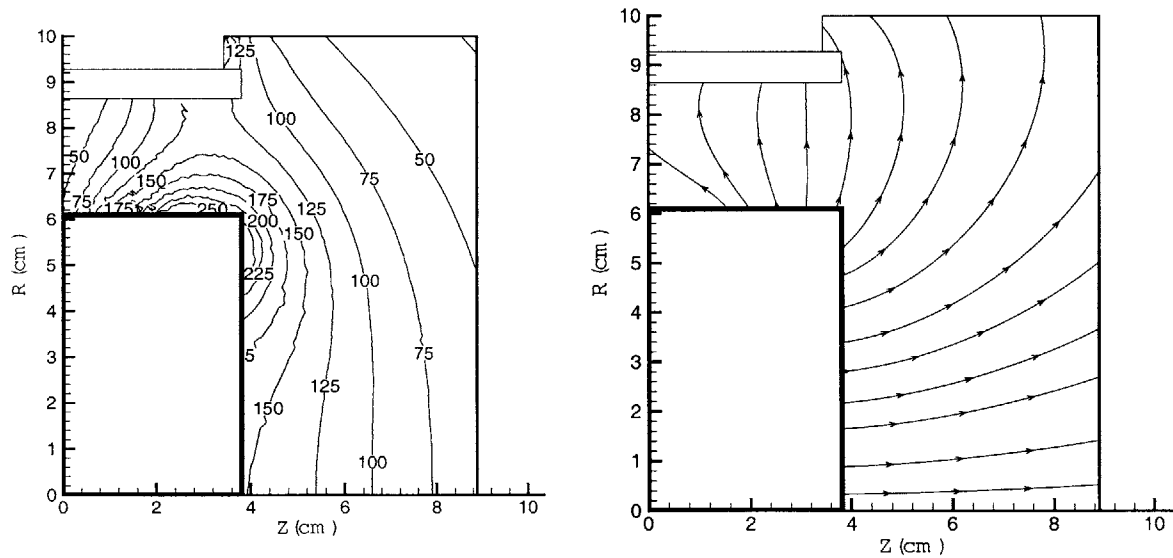Figure 4-1: The P5 thruster geometric configuration

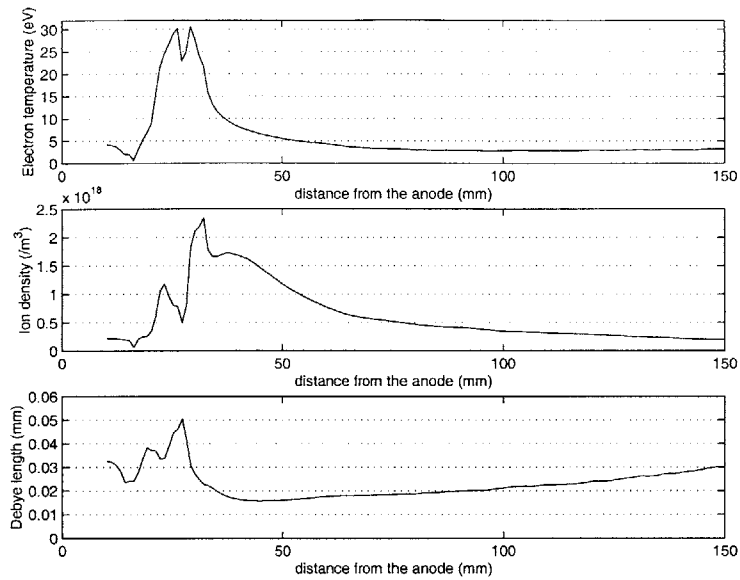Figure 4-2: P5 thruster magnetic field strength (Gauss) and lines

Figure 4-3: P5 internal measurements at chamber mid radius, by James Haas [8]
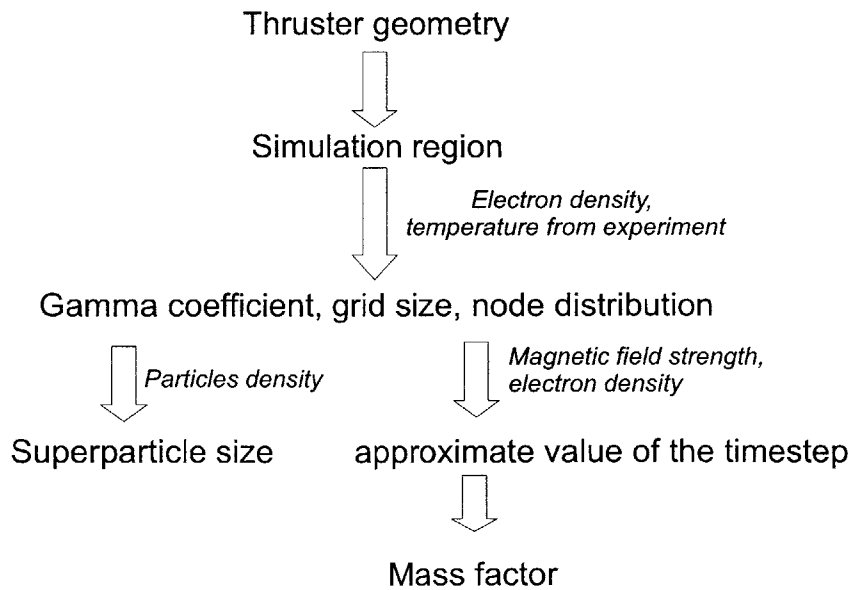

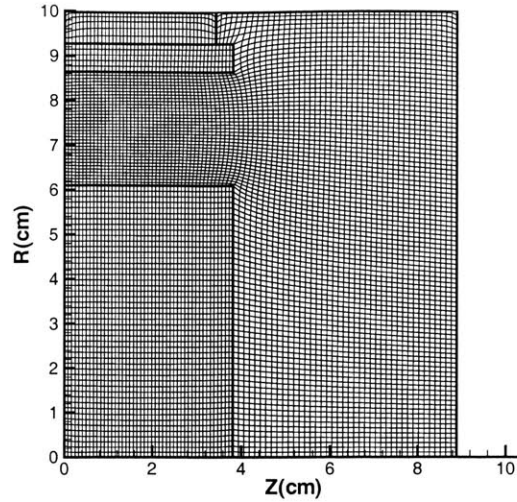Figure 4-4: Reasoning to model a new thruster with the PIC code

Figure 4-5: Basic P5 grid

the mini-TAL.

A reasonable simulation region for the P5 goes from the anode to two channel widths downstream of the channel exit in the axial direction, and from $r = 0$ to half a channel width farther than the channel outer radius in the other dimension. The Debye length requirements are less stringent, but because of the larger geometry, we have about 4000 Debye lengths in the simulation region. That means we need to have a γ coefficient of 50 to use the 88×96 grid shown on Fig. 4-5. This can be seen as a higher distortion of reality, but the modified Debye length, $1\,mm$, remains very small compared to the chamber typical length, $25\,mm$.

A second grid (Fig. 4-6) has been developed, using a 37% finer, cartesian, grid in the chamber, to deal with the high densities generated by oscillations of the code: if a case oscillates deeply, densities can have values 2 to 10 times higher than nominal, decreasing the debye length, and increasing the grid size requirements for the Poisson solver. That grid is coarser in the region outside the thruster however and its size has "only" 108×119 cells.
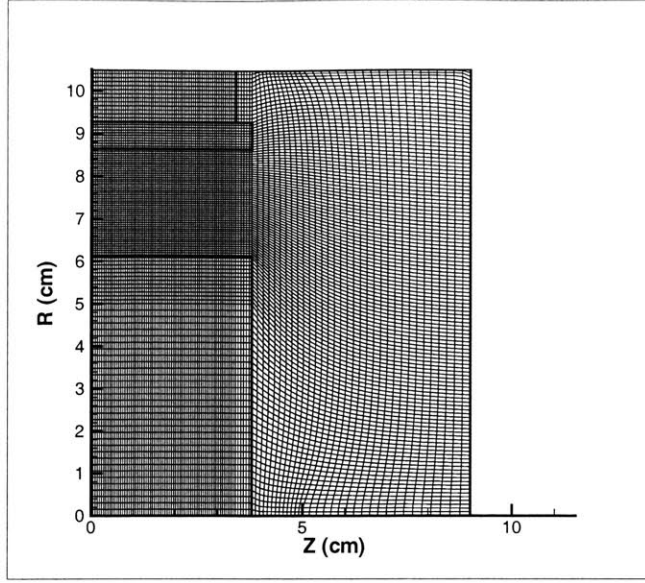
Figure 4-6: Modified P5 grid

4.1.2 Timestep

The magnetic field maximum strength in the P5 peaks at $250G$, 25 times less than the mini-TAL. With a little bit lower perpendicular temperature, the Larmor radius scales with the thruster main dimension.

The Larmor frequency is, for the P5:

$$f_c = \frac{1}{2\pi}\frac{qB}{m_e} \simeq 7.0 \times 10^8 Hz \tag{4.1}$$

The highest computational plasma frequency, with $n_e^{max} = 2.5 \times 10^{12}\, cm^{-3}$, and the artificial permittivity $\gamma = 50$, is:

$$f_p = \frac{1}{\gamma}\frac{1}{2\pi}\sqrt{\frac{e^2 n_e}{m_e \epsilon_0}} \tag{4.2}$$

$$\simeq \frac{1}{\gamma}1.4 \times 10^{10} Hz \simeq 4.4 \times 10^8 Hz \tag{4.3}$$

Unlike the mini-TAL where the gyro-frequency dominated, here, the two frequencies are very similar. The code uses the highest of the two at each iteration to calculate the timestep:

$$\Delta t = 0.3 \times min\left(\frac{1}{f_c}, \frac{1}{f_p}\right) \tag{4.4}$$

69

$$\Delta t \quad \simeq \quad 4.0 \times 10^{-10} s \tag{4.5}$$

4.1.3 Convergence time and mass factor

With the timestep defined above, an axial simulation region length of $10\,cm$ and an average axial speed of $560\,m/s$ for neutrals and $12,800\,m/s$ for ions, the iteration number for convergence is 500,000 for neutrals and 22,000 for ions. These values require a relatively small mass ratio: of the order of 100, to decrease the convergence time by 10.

4.1.4 Superparticle size

In the ionization region, the electron density is $n_e \simeq 2 \times 10^{12}\,cm^{-3}$, the cell main length $0.08\,cm$, the cell volume $.08\pi\,(6.17^2 - 6.1^2) \simeq 0.216\,cm^3$. In order to have 50 electron-superparticles per cell, the superparticle size should be 8.6×10^9.

In the beam outside the channel, $n_e \simeq 5 \times 10^{11}\,cm^{-3}$, and the cell volume is $0.12\pi\,(6.2^2 - 6.1^2) \simeq 0.46\,cm^3$, this means 27 super-electrons per cell.

In the region $1\,cm$ from the axis, $n_e \simeq 5 \times 10^{11}\,cm^{-3}$, the cell volume is $0.12\pi\,(1.2^2 - 1.1^2) \simeq 0.087\,cm^3$, and 5 super-electrons are expected in the cell.

4.2 Ceramic wall modeling

The P5 thruster being an SPT-thruster, most of its walls are made of boron-nitride, which implies new boundary conditions for the electric field and for the particles: secondary emission for instance is likely to be important.

4.2.1 Ceramic wall and Poisson solver

As explained in section 2.2.1, we need at the dielectric boundaries either the potential ϕ or the field normal to the wall $\vec{E}_\perp$. The jump equations for the electric field at a boundary contacting a plasma are:

$$E_{\parallel}^{plasma} - E_{\parallel}^{dielectric} = 0 \tag{4.6}$$
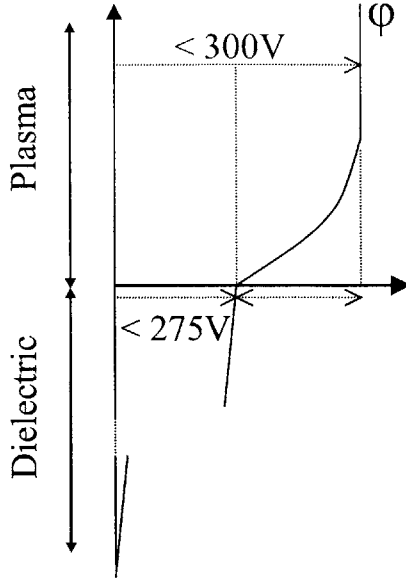
Figure 4-7: Potential differences in the sheath and in the dielectric

$$E_\perp^{plasma} - \underbrace{\epsilon E_\perp^{dielectric}}_{neglected} = \frac{\sigma}{\epsilon_0} \tag{4.7}$$

where σ is the surface charge density, in C/m^2.

In equation (4.7), we are going to neglect $E_\perp^{dielectric}$, as explained below and on Fig. 4-7

In the P5, assuming the electron population is Maxwellian, and $T_i << T_e$, the sheath potential is:

$$\Delta\phi = -\frac{kT_e}{e} \ln 0.654 \sqrt{\frac{T_e + T_i}{T_e} \frac{m_e}{m_i}} \tag{4.8}$$

$$\simeq -6.57 \frac{kT_e}{e} \tag{4.9}$$

This potential difference is applied on a length of the order of a few Debye lengths, about $0.02\,mm$ from 4-3. In the channel, where $T_e > 6\,eV$, $E_\perp^{plasma} > \frac{40V}{3 \times 0.02\,mm} \simeq$ $670,000\,V/m$. Outside the channel, outside the beam, $T_e > 1\,eV$, $E_\perp^{plasma} > \frac{7V}{3 \times 0.02\,mm} \simeq$ $110,000\,V/m$.

On the other side of the boundary, due to the charges accumulated at the surface, the electric field is much less. The dielectric is in contact with the plasma on one side,

and on the other side, or at least in the near vicinity, in contact with the spacecraft, at cathode potential.

That brings the maximum potential difference in the dielectric facing the channel to the potential difference of the thruster, minus what is taken by the sheath: $300 - 30 = 270V$. The dielectric walls being about a cm thick, the electric field near the channel walls in the thruster is therefore maximized by $E_\perp^{dielectric} < \frac{270}{2\,cm} \simeq 14,000\,V/m$. Outside the channel, $E_\perp^{dielectric} < \frac{100}{2\,cm} \simeq 5,000\,V/m$

Finally, bringing everything together, with a dielectric constant of 4 for boron nitride, in the channel:

$$E_\perp^{plasma} > \frac{40\,V}{3 \times 0.02\,mm} \simeq 670,000\,V/m \qquad (4.10)$$

$$\epsilon E_\perp^{dielectric} < 4\frac{270}{2\,cm} \simeq 54,000\,V/m \qquad (4.11)$$

Outside the channel:

$$E_\perp^{plasma} > \frac{7\,V}{3 \times 0.02\,mm} \simeq 110,000\,V/m \qquad (4.12)$$

$$\epsilon E_\perp^{dielectric} < 4\frac{100}{2\,cm} \simeq 20,000\,V/m \qquad (4.13)$$

In both cases, we can neglect $\epsilon E_\perp^{dielectric}$ compared to $E_\perp^{plasma}$.

The implementation of this boundary condition in the code is very simple. Instead of applying analytically the jump relation $E_\perp^{plasma} = \frac{\sigma}{\epsilon_0}$, the code lets charges accumulate at dielectric boundary nodes, and calculates the potential taking these charges into account. In fact, the jump relation itself can be derived from the Gauss' theorem applied to a volume of infinitely small thickness perpendicular to the wall.

4.2.2 Boundary conditions for the particles

Secondary emission yield

Neglecting sputtering, the boundary conditions for neutrals and ions are the same for the dielectric wall as for the metallic walls. For electrons however, secondary emission is not neglected, as it was for metal walls [23, section 2.12.15]. The secondary emission
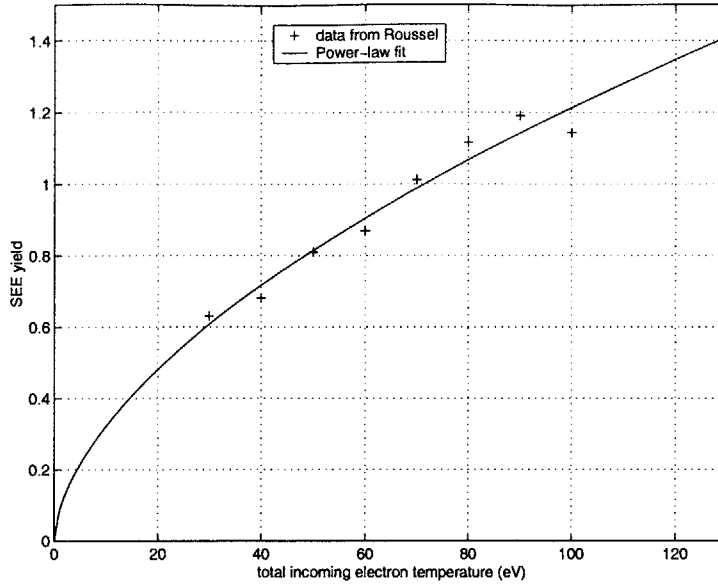
Figure 4-8: Secondary emission yield for BNAlN, from Jolivet and Roussel [11]

rate, estimated from data by Jolivet abd Roussel [11], is presented in Fig. 4-8 for BNAlN. The secondary emission rate δ we use is a power-law fit from Roussel's data:

$$\delta = 0.086 \times E^{0.57} \tag{4.14}$$

where E is the total incoming electron energy, in eV. The total energy is used rather than the perpendicular energy as the roughness of the dielectric surface makes the directionality of the incoming electron unimportant. The crossover $\delta = 1$ takes place at $74\,eV$.

Implementation in the code

The number of emitted electrons per hitting electron is the integer part of δ, plus another electron determined by the comparison of a random number and $\delta - [\delta]$.

The electrons emitted at the boundary are emitted at the collision location, with a half-Maxwellian distribution of $1\,eV$. The value of that energy is not important, as these electrons are accelerated by the sheath before they join the bulk population.

73

4.3 New issues: Bohm diffusion model and sheath magnitude

4.3.1 Bohm diffusion model

In modeling the P5 thruster, we realized that the algorithm previously developed to model the Bohm diffusion had an upper bound for the diffusion it can model. That problem was present in the mini-TAL simulation but had no noticeable effect, as in that thruster, some magnetic lines go from the ionization region to the right-hand-side (Fig. 2-4), enabling electrons to reach the ionization region with no cross-field displacement.

Maximum limit of the collision model

The way Bohm diffusion was implemented in the code is explained in section 2.3.2. The idea is to create the experimental Bohm diffusion $D_\perp = \frac{1}{16}\frac{kT_e}{eB}$ by adding some artificial collisions, that only consist of randomizing the direction of the electron in the plane perpendicular to the B field.

The added collision rate ν_{added} is determined by:

$$D_\perp = \frac{1}{16}\frac{kT_e}{eB} = \frac{kT_e}{m_e}\frac{1}{\omega_c}\frac{\beta}{1+\beta^2} \tag{4.15}$$

where $\beta = \frac{\omega_c}{\nu_{regular}+\nu_{added}}$.

Two limits to the diffusion can be identified:

- ν_{added} has to be much smaller than the inverse of the timestep, as only one "Bohm" collision can be modeled per timestep. As in both the mini-TAL and the P5, the timestep is of the order of $0.3\frac{2\pi}{\omega_c}$, $\nu_{added} < \frac{1}{10} \times \frac{2\pi}{0.3}\omega_c$. The $\frac{1}{10}$ coefficient is used to make sure that the probability that two or more "Bohm" collisions happen during a timestep, $\simeq \left(\frac{1}{10}\right)^2$ is negligible.

That ν gives $\beta_{min} \leq 5.3$ and

$$D_\perp \leq \frac{1}{5.5}\frac{kT_e}{eB} \tag{4.16}$$

74

- there is a maximum of the $\frac{\beta}{1+\beta^2}$ part of equation (4.17). It occurs for $\beta = 1$ and gives a diffusion of

$$D_\perp \leq \frac{1}{2}\frac{kT_e}{eB} \tag{4.17}$$

These two limits are below the experimental constant $\frac{1}{16}$, in $D_\perp = \frac{1}{16}\frac{kT_e}{eB}$; however, we have to multiply that constant by $\sqrt{\text{mass factor}}$, as explained in section 2.5.3. With $\sqrt{\text{mass factor}}$ typically between 30 and 50, we are above the maximum diffusion that can be modeled with the added collision frequency.

Direct diffusion implementation

The best way to bypass that limit for diffusion is model the cross-field diffusion using a Brownian motion. This method is based on the fact that if a particle undergoes a 1D Brownian motion of diffusion D, its position follows a normal distribution of variance $\sigma^2 = 2D_\perp \Delta t$.

After the electron is moved by the leapfrog algorithm, it is moved in the 2D plane perpendicular to the local magnetic field according to a 2D Maxwellian with variance $\sqrt{2D_\perp \Delta t}$:

$$\Delta x = \left[\sqrt{-2\ln\left(\text{random number 1}\right)}\sqrt{2D_\perp \Delta t} \right] cos\left(\text{random number 2}\right) \tag{4.18}$$

$$\Delta y = \left[\sqrt{-2\ln\left(\text{random number 1}\right)}\sqrt{2D_\perp \Delta t} \right] sin\left(\text{random number 2}\right) \tag{4.19}$$

which is then projected back in the (z, r) plane as anyway the θ displacement is not included.

Now that a new location is defined, we have to account for the potential difference between the old location and the new location. We assumed that the anomalous diffusion process conserves energy (that may be arguable, as explained in section 4.4.2), and implemented two ways of conserving it.

The first method assumes that the energy change is limited to the plane perpendicular to the local magnetic field. In this case, the code calculates the initial kinetic energy of the particle in that $B_\perp$ plane, and compares it to the change in potential energy. If the potential energy change is larger than the initial kinetic energy, it

rejects the new location and picks a new Brownian step. If, however, the potential energy change is negative or less than the initial kinetic energy in the $B_\perp$ plane, it updates the magnitude of the 2D velocity according to energy conservation, and picks a direction randomly in that plane. The third component of velocity, parallel to $\vec{B}$ remains unchanged.

The other way of conserving energy is to use the total 3D initial kinetic energy instead of the 2D kinetic energy. The same process as above is used, comparing the potential energy difference to the 3D kinetic energy, and the new velocity has its direction randomized in the 3D space.

This way of modeling anomalous diffusion is computationally slower than the increased collision model, because we have to locate the particle at least twice, but it enables us to model any diffusion magnitude. Particles, when moving up and down along magnetic lines, diffuse slowly across these lines, preferably towards the high potential region, because of energy conservation.

4.3.2 Sheath magnitude

The energy flux to the wall in the PIC code is not correct, because of the artificial mass ratio. That point was not very important in the mini-TAL where the chamber is located near the axis, and hence the wall surface to chamber volume ratio is much smaller, it is much more important for the P5. The first part of this section points out the problem, the second explains how it is solved.

Problem to solve

The sheath magnitude in the code is self-consistent, for metallic walls as for dielectric walls. At the beginning of the simulation, due to their higher speed, more electrons hit the walls. The wall charges negatively, and the sheath builds self-consistently. The sheath magnitude is such that the overall electron and ion flux to the wall is null on average. The charge flux to the wall is determined by the ion flux:

$$j_\perp^- = j_\perp^+ = e n_i v_{bohm} = e n_i \sqrt{\frac{kT_e}{m_i}} \qquad (4.20)$$

76

assuming $T_i \ll T_e$.

The exact value of the sheath for a Maxwellian electron population and for Xenon ions is:

$$\Delta\phi = -\frac{kT_e}{e} \ln 0.654 \sqrt{\frac{T_e + T_i}{T_e} \frac{m_e}{m_i}} \qquad (4.21)$$

$$\simeq -6.57 \frac{kT_e}{e} \exp\left(-\frac{1}{2}\right) \qquad (4.22)$$

The PIC code uses an artificial mass factor to accelerate the convergence, but keeps the plasma density constant. This means that the ion flux to the wall will be higher-than-normal by a ratio $\sqrt{\text{mass factor}}$. This makes sense physically as the ratio of wall velocity to axial velocity has to be preserved: fluxes in all directions scale proportionally to $\sqrt{\text{mass factor}}$. Energy loss by the ions is also correct, as ions make it to the wall independently of their original energy.

From the electron standpoint, the artificial mass factor will weaken the sheath to adjust the electron flux to the wall to the increased ion flux. This scaling is correct as all the electron fluxes have increased in the simulation (see section 2.5.3). On the energy side however, two effects are to be taken into account: the number flux increased but the energy lost per electron decreased, as the sheath magnitude decreased:

$$\Delta\phi^{comp} = -\frac{kT_e}{e} \ln\left(0.654 \sqrt{\frac{T_e + T_i}{T_e} \frac{1}{\text{mass factor}} \frac{m_i}{m_e}}\right) \qquad (4.23)$$

$$= \left(-6.57 + \frac{1}{2} \ln(\text{mass factor})\right) \frac{kT_e}{e} \qquad (4.24)$$

$$= \Delta\phi^{real} + \frac{1}{2} \ln(\text{mass factor}) \frac{kT_e}{e} \qquad (4.25)$$

where $\frac{1}{2} \ln(\text{mass factor}) = 3.4$ for mass factor $= 1000$

This means that now electrons that make it to the sheath are electrons with a minimum energy in the bulk lower than before (Fig. 4-9).

How to solve it

A way to restore the correct sheath magnitude would be to bring the ion flux to the wall back to its real value. This could be done by specularly reflecting some ions
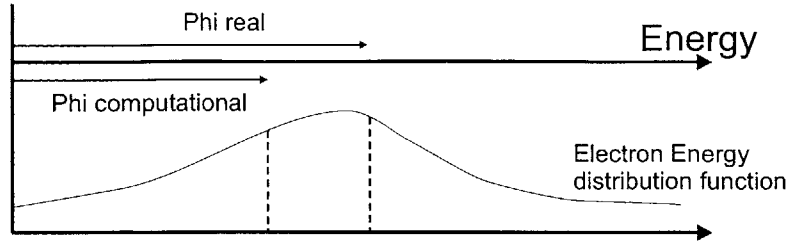
Figure 4-9: Sheath scaling due to the artificial mass factor

hitting the wall with a ratio of $\sqrt{\text{mass factor}}$ reflected for one accepted. That would be be wrong as the number flux has to be higher than in the reality to compensate for the lower ion and neutral mass.

So far, we have the ion number and energy flux correct, and the electron number flux correct. We implemented an electron energy correcting patch, that does not touch the ions, but fixes the lack of electron energy flux to the wall.

When an electron hits the dielectric wall, its total energy E at the wall intersection is calculated. That energy is compared to the difference between the theoretical and the computational Maxwellian sheath magnitude from equations (4.21) and (4.25), using the highest electron temperature computed at the previous iteration and found among the 30 closest cells, starting from the wall, in the perpendicular direction. A coefficient K is used in front of each sheath magnitude, to correct for the fact that the electron population is not Maxwellian, and the sheath formula may overestimate the sheath magnitude. The value of this coefficient is defined at the end of this section, it is initialized at the beginning of the run to be 1.

- if $E > -e\left(K\Delta\phi^{real} - K\Delta\phi^{comp}\right)$

    The electron is "accepted" at the wall, and secondaries are emitted, using the modified energy to calculate the yield: $E + -e\left(K\Delta\phi^{real} - K\Delta\phi^{comp}\right) > 0$.

    The secondaries are emitted with $1\,eV$ of energy as defined in section 4.2.2, plus the amount of energy they should but are not going to get in the sheath: $-e\left(K\Delta\phi^{real} - K\Delta\phi^{comp}\right)$.

78

- else if $E < -e \left(K\Delta\phi^{real} - K\Delta\phi^{comp} \right)$

  This case means that an electron hits the wall, but not the electron "picked" by the code, which had too little energy, and should have stayed in the bulk. Another one, with higher energy, should have made it.

  The electron is specularly reflected, so that it goes back to the bulk, no secondaries are created, but the sheath potential multiplied by K and the collision location are stored for further action.

At the end of the electron loop, the code orders the list of unfulfilled collisions, by region and by energy.

For the P5, 5 regions are created: the channel, the region facing the center dielectric plate, the region facing the upper lip axially, and the region facing the upper lip in the r^+ direction.

The code loops through the electron population, and tries to find electrons in the proper region that have an energy of at least the stored energy (the sheath energy). When a good candidate is found, is is deleted, and secondaries at the dielectric are created with a yield calculated using the excess of energy between the electron energy and the sheath potential.

If at the end of the electron particle loop, some electrons are left to be deleted, the left electrons are just "forgotten", but the code decreases the value of the K coefficient by multiplying it by 0.95. The fact that not enough high-energy electrons are available in the bulk means that the sheath calculated analytically is too strong, and should be decreased. That is the role of K.

4.3.3 Cathode modeling

The role of the cathode is to sustain the discharge and also neutralize the beam. Physically, the cathode is not annular as most components of the thruster; it is located at one single angle, where it creates some plasma (electrons and ions). These electrons drift in the orthoradial $\vec{E} \times \vec{B}$ direction and are therefore available anywhere on a circle centered on the axis and going through the cathode location. Electrons

also move up and down following magnetic lines, and diffuse at a larger timescale perpendicularly to these lines.

Many problems arise when one wishes to model the cathode, as the cathode itself is not in the simulation: where to inject electrons, how many, with what energy?

Originally (see section 2.4), electrons were bounced specularly at the upper free space boundary, to simulate the up and down motion along magnetic lines, and the number of electrons required to match overall neutrality was injected at the free space boundary. Electrons were injected with a half-Maxwellian distribution of low temperature (2.5V), and with a directed energy parallel to the magnetic field corresponding to the energy they should have gained from the field if the potential was positive.

We changed that model towards:

- an "accommodated" specular bouncing at the upper free space boundary, to model the losses to the walls due to electron going all the way along a magnetic line until the thruster wall. The accommodation consists of bouncing specularly the particle, but multiplying the magnitude of its velocity after the bounce by a factor f smaller than 1. This means multiplying the energy by f^2. The value of f is not given theoretically, it is set arbitrarily in the simulation.

- we modified the neutralization procedure to inject electrons in any boundary cell that has a positive charge, using a random number comparison if the net charge is less than 1. This is different from the overall charge neutralyzing used before and closer to the physics, as in reality an excess of positive charges brings the potential up and attracts negative charges, on a length scale of the order of the Debye length. In this new method, if a cell has a potential less than the cathode potential, no electron is injected, whatever the charge in that cell may be: physically, electrons should not be able to make it to negative cells, for energy reasons. The amount of positive charges that accumulate as a result should bring the potential back up self-consistently).

Electrons are injected with no directed energy, and a half-Maxwellian distri-

bution of temperature equal to $\frac{1}{5}$ of the local potential (in eV). Without any losses, electrons should gain $\frac{2}{5}$ of the potential, here, $\frac{1}{5}$ is used instead to account for losses that would have happened outside the simulation.

4.4 First results

4.4.1 Results with low diffusivity

The only case that converged is paradoxically a case with very small diffusion. The actual Bohm diffusion coefficient used is $D_\perp = \frac{1}{6400}\frac{kT_e}{eB}$.

Boundary conditions used for the Poisson solver are $\phi = 0$ at the upper right-hand-side corner, and $E \perp = 0$ at the free space boundaries, except if that implies that the potential gets to a value 10 Volts or more below the cathode potential, in which case the potential is set to be $\phi_{cathode} - 10\,V$ (method explained in 2.2.1). Ions and neutrals are free to leave through the free space boundary, while the electrons are bounced specularly at the upper free space boundary, and are free to leave though the right-hand-side exit plane (beam).

The cathode is modeled as explained in 4.3.3. The cathode current in this geometry cannot be computed, because electrons that would be considered coming from the cathode can come from the upper-free-face boundary bouncing or from the right-hand-side injection; they can not be identified.

Ionization oscillations

This run undergoes very deep ionization oscillation, which are characterized by a numerical frequency of $421\,kHz$. Incidentally, the ion density at the exit of the chamber is varying from $10^{11}\,cm^{-3}$ to $10^{12}\,cm^{-3}$. The very small cross-field diffusion is compensated by the presence of a steady population of electrons moving back and forth along magnetic field lines (Fig. 4-2) - right in front of the exit of the chamber. This population is bounded at the upper side by the specular bouncing boundary, and at the lower side by the sheath potential created self-consistently at the dielectric
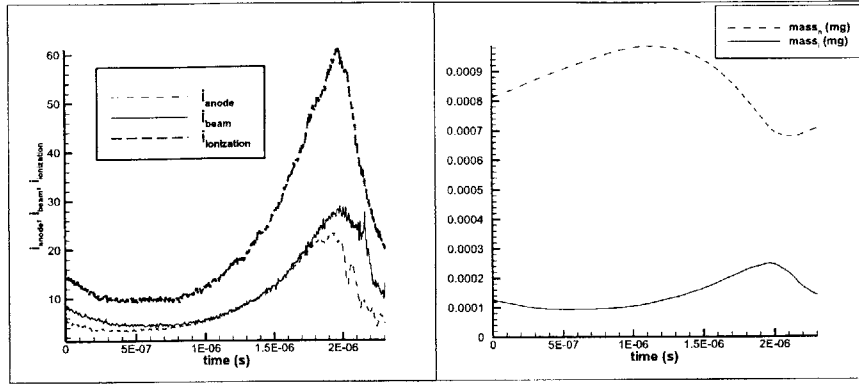
Figure 4-10: Ionization, beam and anode current (A); Ion and neutral mass in the simulation (mg) over an oscillation

boundary. With little cross-field diffusion these electrons move up and down along the magnetic lines, and they are always available to "reseed" the chamber at an ionization minimum.

The oscillation frequency seems to agree well with the predator-prey theory: the observed frequency is $421\,kHz$, when it is expected to be

$$f = \tfrac{1}{2\pi}\Omega = \tfrac{\sqrt{V_i V_n}}{2\pi L} \tag{4.26}$$

where V_i is the average axial ion velocity in the chamber, approximated by half the energy of an ion accelerated by $300\,V$ of potential. V_n in the chamber is about $1/20$ smaller than V_i, hence:

$$f = \frac{\sqrt{250,000\,m/s \times 12,500\,m/s}}{2\pi \times 0.02\,m} \tag{4.27}$$

All these velocities are $\sqrt{\text{Mass}}$ factor too large; to compare with experiments, we need to decrease the speed of neutrals and ions, hence

$$f \simeq \tfrac{445\,kHz}{\sqrt{1,000}} = 14\,kHz \tag{4.28}$$

which is close to the experimental value of 11kHz measured by Haas [8].

Thrust and efficiency calculations

Calculated thrust, and Isp are within 15% to those measured by James Haas [8] as shown on Table 4.4.1. Moreover, the thrust, once corrected for the larger mass flow

	Code	Measured
Thrust (mN)	207	180
Isp (s)	1846	1650
I_{anode} (A)	8.80	10.0
Efficiency	0.76	0.48

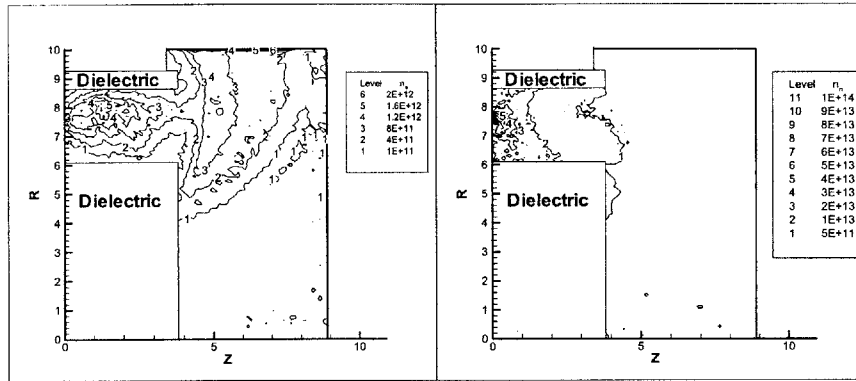Table 4.1: Measured and calculated P5 parameters

Figure 4-11: Electron and neutral density near oscillation peak (cm^{-3})

used in this computation (11.41 mg/s), is within 5% of the actual measurements. The overall efficiency departs from experimental values because of the low current in the simulation, reflecting the low anomalous diffusion coefficient used.

Calculated utilization efficiency is very high - 0.93. This is probably due to the presence of the ring of electrons at the exit of the thruster that can be considered as a second ionization zone. Interestingly enough, a quite high fraction of double ions (0.28) is observed. This double ion population has an axial energy at the exit of the thruster only 1.10 times higher than that of the single ions. These double ions are not present inside the chamber, they are mostly created in the ring of electrons in front of exit of the chamber (Fig. 4-12). The potential at this location is very low, compared to the applied anode voltage, and this explains the relative low speed of the double ions.

From Fig. 4-11 one can see that neutral density decay and hence ionization, takes place towards the exit of the chamber; electron density peaks near the channel exit
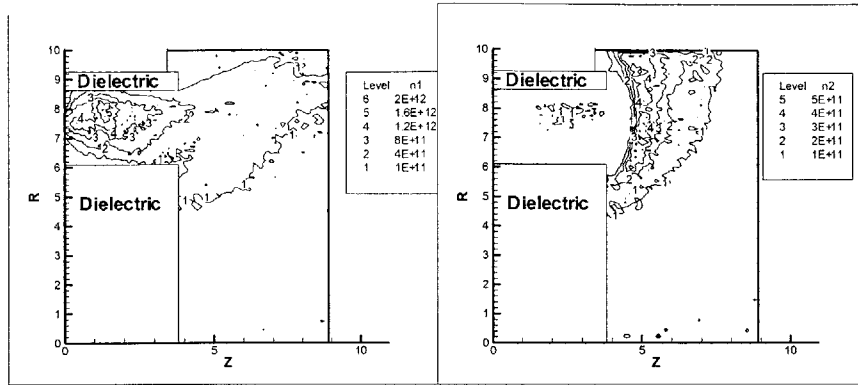
Figure 4-12: Single and double ion density near oscillation peak (cm^{-3})
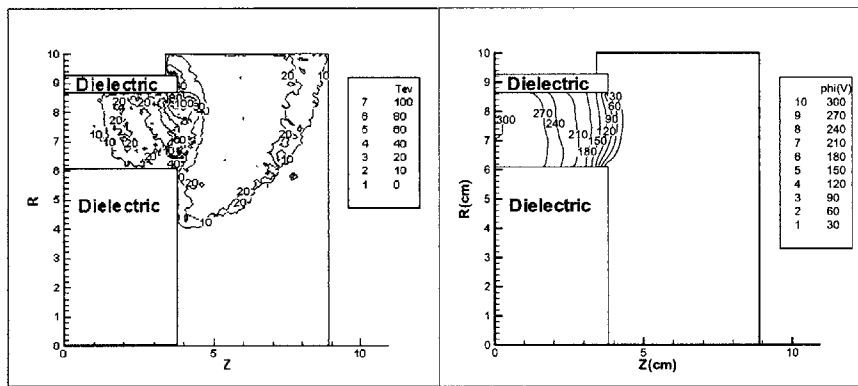
Figure 4-13: Electron temperature (eV) and electric potential (V)

during a peak of ionization and moves back towards the anode at a low ionization time. The electric potential (Fig. 4-13) demonstrates a similar behavior.

4.4.2 Results with correct diffusivity

Fig. 4-14 shows a snapshot of electron density from a case with a larger diffusion $(D_\perp = \frac{1}{400} \frac{kT_e}{eB})$. Although this case does not converge and dies after several ionization oscillations, the intermediate results are in good accordance with experiments in terms of plasma density (Fig. 4-14). The ring of electrons at the exit of the chamber is not formed, and the density inside the chamber matches the experiments (Fig. 4-14): there is a low peak close to the anode followed by a larger peak of density in the

channel.

This case shows very high electron temperatures at the exit of the chamber (Fig. 4-15), compared to experiments (Fig. 4-14), upper curve on the right side). This high temperature may be responsible for the deep diverging oscillations of the code, as it represents a very high amount of energy available for ionization: an electron with $100\,eV$ of energy can ionize 3 times more neutrals than an electron with $30\,eV$. The reason for these high temperatures may be the anomalous diffusion algorithm, which is responsible for most of the electron energy gain from the field. Two processes could be involved:

- The value of the anomalous diffusion may not be constant. Capelli, from Stanford University, measured a diffusion value 10 times lower in the chamber than in the beam.

- In the current anomalous diffusion algorithm, diffusion is modeled as a Brownian motion, where energy is conserved. The algorithm decides a new location for the particle, and calculates the potential energy difference between the old and the new location. If the location is "forbidden" (i.e. the potential energy difference is larger than the kinetic energy at the old location), a new location is picked. If not, the new magnitude of the velocity is calculated, and its direction randomized. However, there is a possibility that the plasma fluctuations responsible for electron anomalous diffusion may be growing in the crucial regions at the expense of electron energy. This is an area where much more detailed physical research is needed.
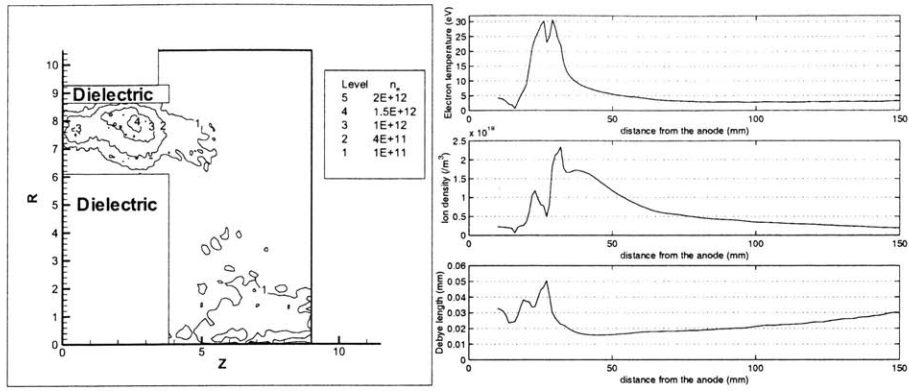
Figure 4-14: Time-averaged electron density (cm^{-3}) with higher anomalous diffusion, and electron density and temperature profiles at mid-channel from experiments
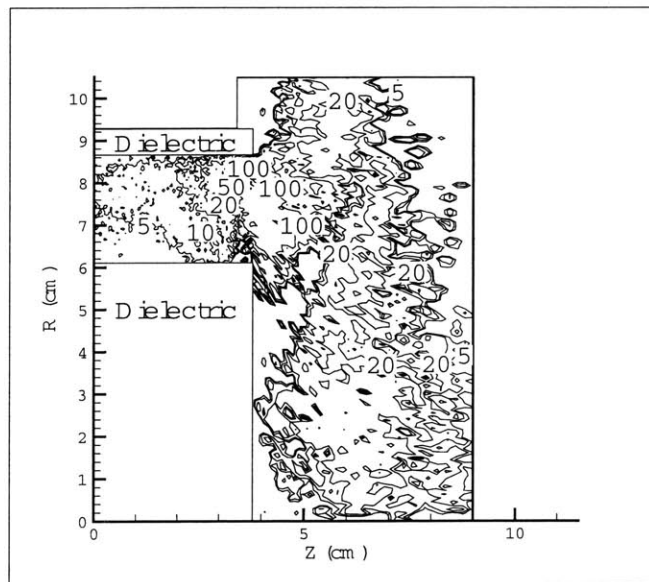

Figure 4-15: Time-averaged electron temperature (eV) with higher anomalous diffusion

86

Chapter 5

Conclusions

We have carried out a numerical exploration with a fully kinetic PIC code of the effects of raising the operating potential in a miniature TAL thruster. The results appear to validate the usefulness of this numerical tool for identifying detailed trends and effects. Among the important results of our work, we can mention: the calculation of the optimum magnetic field at each voltage, the existence of a maximum efficiency if the magnetic field is not optimized, the disappearance (or near disappearance) of this maximum when the magnetic field is optimized, the nearly linear increase of electron temperature with voltage, the spatial separation of the two channels for double ion formation, with one of them predominating in the low-potential central spike, the identification of most of the detailed mechanisms for efficiency variation, through a detailed analysis of its constitutive factors.

We further modified the PIC code to model a 3kW class SPT thruster. We obtained converged results with lower-than-nominal diffusion. The overall thrust, specific impulse and oscillation frequency are in good accordance with measurements, but internal densities map, ionization strength and currents differ from experiments, reflecting the low anomalous diffusion used. Some preliminary results with higher diffusion values were obtained. They show good agreement for plasma density maps, but do not converge in the long run, and present high temperatures in the beam region. We expect this is due to the diffusion model used.

We recommend further work on the diffusion model to achieve full-convergence of

the SPT model. The anomalous diffusion may differ from the classic $D_\perp = \frac{1}{16}\frac{kT_e}{eB}$ towards larger values in the beam and lower values in the chamber, while the anomalous diffusion process is probably not an energy-conserving process. Further work on the model should also include higher-order Xenon ionization, ion excitation, ionization through metastables and wall sputtering.

Appendix A

Breaking up the anode efficiency

The overall efficiency of a Hall thruster, also called anode efficiency is defined by:

$$\eta = \frac{T^2}{2\dot{m}UI} \tag{A.1}$$

where I is the cathode/anode current. It can be expressed as a function of the beam current:

$$I = \frac{I_{beam}}{\eta_e} \tag{A.2}$$

where η_e is the electrical efficiency, and I_{beam} the ion beam current

$$I_{beam} = \frac{e}{m_i}(\dot{m}^+ + 2\dot{m}^{++}) \tag{A.3}$$

The thrust and the current in Eq. (A.1) can be expressed as a function of the mass flows and average axial velocities of the different species: neutrals, single and double ions.

$$\eta = \eta_e \frac{(\dot{m}^+\bar{v}_z^+ + \dot{m}^{++}\bar{v}_z^{++} + \dot{m}^n\bar{v}_z^n)^2}{\frac{2\dot{m}Ue}{m_i}(\dot{m}^+ + 2\dot{m}^{++})} \tag{A.4}$$

This can also be written as

$$\eta = \eta_e \frac{m_i(\bar{v}_z^+)^2}{2Ue} \frac{\left(\frac{\dot{m}^+}{\dot{m}} + \frac{\dot{m}^{++}}{\dot{m}}\frac{\bar{v}_z^{++}}{\bar{v}_z^+} + \frac{\dot{m}^n}{\dot{m}}\frac{\bar{v}_z^n}{\bar{v}_z^+}\right)^2}{\left(\frac{\dot{m}^+}{\dot{m}} + 2\frac{\dot{m}^{++}}{\dot{m}}\right)} \tag{A.5}$$

Introducing the acceleration and dispersion efficiency for the single ions,)

$$\eta_a^+ = \frac{\dot{m}^+ (\bar{v}^+)^2}{2Ue} \tag{A.6}$$

$$\eta_d^+ = \left(\frac{\bar{v}_z^+}{\bar{v}^+}\right)^2 \tag{A.7}$$

equation (A.4) becomes

$$\eta = \eta_e \eta_a^+ \eta_d^+ \frac{\left(\frac{\dot{m}^+}{\dot{m}} + \frac{\dot{m}^{++}}{\dot{m}}\frac{\bar{v}_z^{++}}{\bar{v}_z^+} + \frac{\dot{m}^n}{\dot{m}}\frac{\bar{v}_z^n}{\bar{v}_z^+}\right)^2}{\frac{\dot{m}^+}{\dot{m}} + 2\frac{\dot{m}^{++}}{\dot{m}}} \tag{A.8}$$

The utilization efficiencies for the single and double ions is defined by

$$\eta_u^+ = \frac{\dot{m}^+}{\dot{m}} \tag{A.9}$$

$$\eta_u^{++} = \frac{\dot{m}^{++}}{\dot{m}} \tag{A.10}$$

To characterize the acceleration and the dispersion of the neutrals and double ions, we introduce two parameters β^+ and β^{++},

$$\beta^{++} = \frac{\bar{v}_z^{++}}{\bar{v}_z^+} \tag{A.11}$$

$$\beta^n = \frac{\bar{v}_z^n}{\bar{v}_z^+} \tag{A.12}$$

Including these coefficients in η,

$$\eta = \eta_e \eta_a^+ \eta_d^+ \frac{(\eta_u^+ + \eta_u^{++}\beta^{++} + \eta_u^n\beta^n)^2}{(\eta_u^+ + 2\eta_u^{++})} \tag{A.13}$$

This equation can be simplified for simulations with no double ions and negligible neutral velocity:

$$\eta = \eta_e \eta_a^+ \eta_d^+ \eta_u^+ \tag{A.14}$$

For the case with double ions, η can be expressed in a similar way if we define an efficient utilization η_u^{eff}:

$$\eta = \eta_e \eta_a^+ \eta_d^+ \eta_u^{\text{eff}} \tag{A.15}$$

$$\eta_u^{\text{eff}} = \frac{(\eta_u^+ + \eta_u^{++}\beta^{++} + \eta_u^n\beta^n)^2}{\eta_u^+ + 2\eta_u^{++}} \tag{A.16}$$

Appendix B

Functions *consolidate()* and *gauss_dielectric()*

B.1 *consolidate()*

```
/* ————————————————————————————*/
/* this function consolidates the Gauss constants*/
/* ————————————————————————————*/
void consolidate_VB(void){

        int k, j, k1,j1,k2,j2;
        double North, South, East, West;
        double N2,S2,E2,W2;
        double N3,S3,E3,W3;
        struct aardvark temp;                                    10


        for (k=0;k<=N_Z−1;k++) {
                for (j=0;j<=N_R−1;j++){


                        k1=k;
```

91

```
j1=j;

constant[k][j].c  =0;

constant[k][j].n  =0;

constant[k][j].ne=0;                                         20

constant[k][j].e  =0;

constant[k][j].se=0;

constant[k][j].s  =0;

constant[k][j].sw=0;

constant[k][j].w  =0;

constant[k][j].nw=0;


if (grid[k][j].cell==INTERIOR&&k<N_Z−1&&j<N_R−1){
        //NE corner
        k2=k+1;                                              30
        j2=j+1;
        temp=gauss_dielectric(k1,j1,k2,j2);
        constant[k][j].c  −=temp.c  *e_o;
        constant[k][j].n  +=temp.n  *e_o;
        constant[k][j].ne+=temp.ne*e_o;
        constant[k][j].e  +=temp.e  *e_o;
}


if (grid[k][j−1].cell==INTERIOR&&k<N_Z−1&&j>0){
        //SE corner                                          40
        k2=k+1;
        j2=j−1;
        temp=gauss_dielectric(k1,j1,k2,j2);
        constant[k][j].c  −=temp.c  *e_o;
        constant[k][j].s  +=temp.n  *e_o;
        constant[k][j].se+=temp.ne*e_o;
```

```
                    constant[k][j].e +=temp.e *e_o;

          }
          if (grid[k−1][j−1].cell==INTERIOR&&k>0&&j>0){
                    //SW corner                                    50
                    k2=k−1;
                    j2=j−1;
                    temp=gauss_dielectric(k1,j1,k2,j2);
                    constant[k][j].c −=temp.c *e_o;
                    constant[k][j].s +=temp.n *e_o;
                    constant[k][j].sw+=temp.ne*e_o;
                    constant[k][j].w +=temp.e *e_o;
          }
          if (grid[k−1][j].cell==INTERIOR&&k>0&&j<N_R−1){
                    //NW corner                                    60
                    k2=k−1;
                    j2=j+1;
                    temp=gauss_dielectric(k1,j1,k2,j2);
                    constant[k][j].c −=temp.c *e_o;
                    constant[k][j].n +=temp.n *e_o;
                    constant[k][j].nw+=temp.ne*e_o;
                    constant[k][j].w +=temp.e *e_o;
          }


     }                                                             70
   }
 }
```

B.2 gauss_dielectric()

```
/* ————————————————————————*/
/* Function to calculate the grid constants for the poisson solver*/
/* ————————————————————————*/
struct aardvark gauss_dielectric(int k1, int j1, int k2, int j2 ) {

        struct aardvark constant;
        struct weather tangent, punkt;
        struct point_zr norm;
        double aria;
        double half_top, half_right;                                    10
        int sign_k, sign_j;



        /*We are gonna do everything as if we were dealing with a NE corner.
        the cnneter is (k1, j1) and the NE point (k2,j2)
        the only thing we need to change if it is not the case is
        *change the normal signs for the SE and NW corners
        why? when "turning" clockwise, the tangent is always pointing out of the box*/


                                                                        20

        //first initialize the constant. all we need is n, ne, e and c as we are
        //doing as if we had a NE corner.


        constant.n =0.0;
        constant.ne=0.0;
        constant.e =0.0;
        constant.c=0.0;
        half_right=(k1+k2)/2.0;
```

94

```
half_top   =(j1+j2)/2.0;

punkt.n  =comp_2_real(k1,half_top);
punkt.ne=comp_2_real(half_right,half_top);
punkt.e  =comp_2_real(half_right,j1);


sign_k=k2−k1;
sign_j=j2−j1;



//first the NNE face
//need the area and the normal to the surface vector
aria=area(punkt.n, punkt.ne); //always positive
norm=get_normal(punkt.n,punkt.ne);
//make sure the normal vector points outside
if ( (k2−k1)*(j2−j1)!=1) {
        norm.z=−norm.z;

        norm.r=−norm.r;

}


norm.z*=aria;

norm.r*=aria;



tangent.w.z = 0.5 *(  grid[k1][j1].deta_dz + grid[k1][j2].deta_dz);
tangent.w.r = 0.5 *(  grid[k1][j1].deta_dr + grid[k1][j2].deta_dr);
tangent.e.z = 0.5 *(  grid[k2][j1].deta_dz + grid[k2][j2].deta_dz);
tangent.e.r = 0.5 *(  grid[k2][j1].deta_dr + grid[k2][j2].deta_dr);
tangent.s.z = 0.25*(3*grid[k1][j1].dxi_dz  + grid[k2][j1].dxi_dz );
tangent.s.r = 0.25*(3*grid[k1][j1].dxi_dr  + grid[k2][j1].dxi_dr );
```

```
tangent.n.z = 0.25*(3*grid[k1][j2].dxi_dz  + grid[k2][j2].dxi_dz );
tangent.n.r = 0.25*(3*grid[k1][j2].dxi_dr  + grid[k2][j2].dxi_dr );          60


//now needs to add all the terms:


constant.n  += ( .75*sign_j*tangent.w.z − .5*sign_k*tangent.n.z)*norm.z;
constant.n  += ( .75*sign_j*tangent.w.r − .5*sign_k*tangent.n.r)*norm.r;
constant.ne+= ( .25*sign_j*tangent.e.z + .5*sign_k*tangent.n.z)*norm.z;
constant.ne+= ( .25*sign_j*tangent.e.r + .5*sign_k*tangent.n.r)*norm.r;
constant.e  += (−.25*sign_j*tangent.e.z + .5*sign_k*tangent.s.z)*norm.z;
constant.e  += (−.25*sign_j*tangent.e.r + .5*sign_k*tangent.s.r)*norm.r;
constant.c  += (−.75*sign_j*tangent.w.z − .5*sign_k*tangent.s.z)*norm.z; 70
constant.c  += (−.75*sign_j*tangent.w.r − .5*sign_k*tangent.s.r)*norm.r;


//second the ENE face


aria=area(punkt.ne, punkt.e);
norm=get_normal(punkt.ne,punkt.e);
//make sure the normal vector points outside
if ( (k2−k1)*(j2−j1)!=1 {                                                    80
        norm.z=−norm.z;
        norm.r=−norm.r;
}


norm.z*=aria;
norm.r*=aria;


tangent.w.z = 0.25 *(3*grid[k1][j1].deta_dz + grid[k1][j2].deta_dz);
```

96

```
tangent.w.r = 0.25 *(3*grid[k1][j1].deta_dr + grid[k1][j2].deta_dr);
tangent.e.z = 0.25 *(3*grid[k2][j1].deta_dz + grid[k2][j2].deta_dz);     90
tangent.e.r = 0.25 *(3*grid[k2][j1].deta_dr + grid[k2][j2].deta_dr);
tangent.s.z = 0.5  *(  grid[k1][j1].dxi_dz  + grid[k2][j1].dxi_dz );
tangent.s.r = 0.5  *(  grid[k1][j1].dxi_dr  + grid[k2][j1].dxi_dr );
tangent.n.z = 0.5  *(  grid[k1][j2].dxi_dz  + grid[k2][j2].dxi_dz );
tangent.n.r = 0.5  *(  grid[k1][j2].dxi_dr  + grid[k2][j2].dxi_dr );


constant.n += (-.25*sign_k*tangent.n.z + .5 *sign_j*tangent.w.z)*norm.z;
constant.n += (-.25*sign_k*tangent.n.r + .5 *sign_j*tangent.w.r)*norm.r;
constant.ne+= ( .25*sign_k*tangent.n.z + .5 *sign_j*tangent.e.z)*norm.z;
constant.ne+= ( .25*sign_k*tangent.n.r + .5 *sign_j*tangent.e.r)*norm.r; 100
constant.e += ( .75*sign_k*tangent.s.z - .5 *sign_j*tangent.e.z)*norm.z;
constant.e += ( .75*sign_k*tangent.s.r - .5 *sign_j*tangent.e.r)*norm.r;
constant.c += (-.75*sign_k*tangent.s.z - .5 *sign_j*tangent.w.z)*norm.z;
constant.c += (-.75*sign_k*tangent.s.r - .5 *sign_j*tangent.w.r)*norm.r;


return constant;
}
```

Bibliography

[1] E. Ahedo, P. Martinez-Cerezo, J.M. Gallardo, and M. Martinez-Sanchez. Characterization of the plasma in a Hall thruster. *IEPC-01-17, 27th International Electric Propulsion Conference, Pasadena, CA*, October 2001.

[2] S. Barral, Z. Peradzyński, and K. Makowski. About the double-humped electron distribution function in Hall thrusters. *IEPC-01-25, 27th International Electric Propulsion Conference, Pasadena, CA*, October 2001.

[3] M.B. Belikov, O.A. Gorskov, and R.N. Rizakhanov. Investigation on a Hall thruster of 1.5kw class at specific impulses up to 3000s. *AIAA-2000-3253m, 36th Joint Propulsion Conference, Huntsville, AL*, July 2000.

[4] V. Blateau, M. Martinez-Sanchez, O. Batishchev, and J. Szabo. PIC simulation of high specific impulse Hall effect thruster. *IEPC-01-037, 27th International Electric Propulsion Conference, Pasadena, CA*, October 2001.

[5] Birdsall C.K. and A.B. Langdon. *Plasma physics via Computer Simulation*. Institute of Physics Publishing, Bristol and Philadelphia, 1991.

[6] J.M. Fife. *Hybrid-PIC modeling and electrostatic probe survey of Hall trhusters*. PhD thesis, MIT, 1998.

[7] J. S. Gulczinski. *Examination of the structure and evolution of ion energy properties of a 5kW class laboratory Hall effect thruster at various operational conditions*. PhD thesis, University of Michigan, 1999.

[8] J. Haas. *Low-Perturbation Interrogation of the Internal and Near-Field Plasma Structure of a Hall Thruster Using a High-Speed Probe Positioning System.* PhD thesis, University of Michigan, 2001.

[9] M. Hayashi. Determination of electron-xenon total excitation cross-sections, from threshold to 100 eV, from experimental values of Townsend's α.

[10] D.T. Jacobson, R.S. Jankovsky, V.K. Rawlin, and D.H. Manzella. High voltage TAL performance. *AIAA-2001-3777, 37th Joint Propulsion Conference, Salt Lake City, UT*, July 2001.

[11] L. Jolivet and J.-F. Roussel. Effects of the secondary electron emission on the sheath phenomenon in a Hall thruster. *3rd International Conference on Spacecraft Propulsion, Cannes, France*, October 2000.

[12] V. Khayms. Preliminary experimental evaluation of a miniaturized Hall thruster. *IEPC-97-077, 25th International Electric Propulsion Conference*, 1997.

[13] D.H. Manzella, D.T. Jacobson, and R.S. Jankowsky. High voltage SPT performance. *AIAA-2001-3774, 37th Joint Propulsion Conference, Salt Lake City, UT*, July 2001.

[14] R. Nogushi, M. Martinez-Sanchez, and E. Ahedo. Linear 1-D analysis of oscillations in Hall thrusters. *IEPC-99-105, 26th International Electric Propulsion Conference, Kitakyushu, Japan*, October 1986.

[15] D. Oh. *Computational Modeling of Expanding Plasma Plumes in Space using a PIC-DSMC Algorithm.* PhD thesis, MIT, 1997.

[16] S. Oleson and J.M. Sankovic. Advanced Hall electric propulsion for futur in-space transportation. *IEPC-97-077, 25th International Electric Propulsion Conference*, 1997.

[17] B. Pote. Performance of a high specific impulse Hall thruster. *IEPC-01-35, 27th International Electric Propulsion Conference, Pasadena, CA*, October 2001.

[18] C. Ramsauer. Uber den Wirkungsquerschnitt der Gasmoleküle langsamen Elektronen. II. Fortsetzung und Schluss. *Ann. d. Physik*, 72:345, 1923.

[19] C. Ramsauer and R. Kollath. Uber den Wirkungsquerschnitt der Edelgasmoleküle gegenüber Elektronen unterhalb 1 Volt. *Ann. d. Physik*, 3:536, 1929.

[20] D. Rapp and P. Englander-Golden. Total cross sections for ionization and attachment in gases by electron impact. I. Positive ionization. *Journal of Chemical Physics*, 43(5), 1965.

[21] D. Rapp and W.E. Francis. Charge exchange between gaseous ions and atoms. *Journal of Chemical Physics*, 37(11):2631-2645, 1962.

[22] J.J Szabo. Fully kinetic Hall thruster modeling. *IEPC-01-341, 27th International Electric Propulsion Conference, Pasadena, CA*, October 2001.

[23] J.J. Szabo. *Fully Kinetic Numerical Modeling of a Plasma Thruster*. PhD thesis, MIT, January 2001.

[24] J.J. Szabo, M. Martinez-Sanchez, and O. Batishchev. Numerical modeling of the near-anode region of a TAL thruster. *AIAA 2000-3653, 36th Joint Propulsion Conference, Huntsville, AL*, July 2000.

[25] J.J. Szabo, M. Martinez-Sanchez, and J. Moheiser. Application of 2-D hybrid code to alternative Hall thruster geometries. *AIAA-98-3795, 34th AIAA Joint Propulsion Conference*, July 1998.